# Localization of Usher 1 proteins to the photoreceptor calyceal processes, which are absent from mice

Iman Sahly,[1,3,4] Eric Dufour,[1,3,4] Cataldo Schietroma,[1,3,4] Vincent Michel,[2,3,4] Amel Bahloul,[2,3,4] Isabelle Perfettini,[2,3,4] Elise Pepermans,[2,3,4] Amrit Estivalet,[1,3,4] Diane Carette,[2,3,4] Asadollah Aghaie,[1,3,4] Inga Ebermann,[2,3,4] Andrea Lelli,[2,3,4] Maria Iribarne,[2,3,4] Jean-Pierre Hardelin,[2,3,4] Dominique Weil,[2,3,4] José-Alain Sahel,[1,5] Aziz El-Amraoui,[2,3,4] and Christine Petit[1,2,3,4,6]

[1]Institut de la vision, Syndrome de Usher et autres Atteintes Rétino-Cochléaires, 75012 Paris, France
[2]Institut Pasteur, Unité de Génétique et Physiologie de l'Audition, 75724 Paris, Cedex 15, France
[3]INSERM UMRS 587, 75015 Paris, France
[4]Université Pierre et Marie Curie (Paris VI), 75005 Paris, France
[5]Institut de la Vision, Département de Génétique, INSERM UMRS 968, 75012 Paris, France
[6]Collège de France, 75231 Paris, Cedex 05, France

The mechanisms underlying retinal dystrophy in Usher syndrome type I (USH1) remain unknown because mutant mice lacking any of the USH1 proteins—myosin VIIa, harmonin, cadherin-23, protocadherin-15, sans—do not display retinal degeneration. We found here that, in macaque photoreceptor cells, all USH1 proteins colocalized at membrane interfaces (i) between the inner and outer segments in rods and (ii) between the microvillus-like calyceal processes and the outer segment basolateral region in rods and cones. This pattern, conserved in humans and frogs, was mediated by the formation of an USH1 protein network, which was associated with the calyceal processes from the early embryonic stages of outer segment growth onwards. By contrast, mouse photoreceptors lacked calyceal processes and had no USH1 proteins at the inner–outer segment interface. We suggest that USH1 proteins form an adhesion belt around the basolateral region of the photoreceptor outer segment in humans, and that defects in this structure cause the retinal degeneration in USH1 patients.

## Introduction

Usher syndrome (USH) is the most frequent cause of inherited dual hearing and visual sensory impairment. Three types of USH (USH1, USH2, and USH3), caused by different gene defects, have been distinguished clinically. USH1 is the most severe form in terms of both the extent of the sensorineural hearing impairment and the precocity of retinitis pigmentosa onset. Over the last 16 years, a wealth of data enlightening the roles of the USH1 proteins—myosin VIIa (USH1B), harmonin (USH1C), cadherin-23 (USH1D), protocadherin-15 (USH1F), and sans (USH1G)—in the auditory sensory cells (hair cells) has been obtained, mostly through studies of mice carrying mutations in the five orthologous genes. These mutant mice (Ush1 mice) indeed faithfully mimic the human hearing impairment. All five USH1 proteins have been shown to play an essential role in the growing and mature hair bundle (Fig. S1 A), the mechanoreceptive structure by which hair cells respond to sound-evoked mechanical stimuli. Early in the growth of the hair bundle, USH1 proteins form transient fibrous links that ensure hair bundle cohesiveness, by interconnecting the stereocilia, stiff microvilli, together and the kinocilium, a genuine cilium, to stereocilia (Lefèvre et al., 2008). USH1 proteins subsequently form the core of the mechano-electrical transduction machinery that converts acoustic energy into an electrical receptor potential (Kazmierczak et al., 2007; Grillet et al., 2009; Michalski et al., 2009; Caberlotto et al., 2011; Grati and Kachar, 2011).

By contrast, the pathogenesis of the retinitis pigmentosa observed in USH1 remains elusive. This retinopathy is classified as a rod–cone dystrophy, in which rod dysfunction occurs

I. Sahly, E. Dufour, C. Schietroma, and V. Michel contributed equally to this paper.

Correspondence to Aziz El-Amraoui: aziz.el-amraoui@pasteur.fr; or Christine Petit: christine.petit@pasteur.fr

Abbreviations used in this paper: RLI, relative labeling index; RT-qPCR, RT-quantitative PCR; USH, Usher syndrome.



The Rockefeller University Press $30.00
J. Cell Biol. Vol. 199 No. 2 381–399
www.jcb.org/cgi/doi/10.1083/jcb.201202012

first and rapidly worsens, whereas cone dysfunction and degeneration lag behind and progress more slowly (Williams et al., 2009; Malm et al., 2011a,b). Abnormal electroretinographic responses are recorded in patients from the earliest age at which the tests have been performed, 18 months (Flores-Guevara et al., 2009; Williams et al., 2009; Jacobson et al., 2011; Malm et al., 2011a,b). Strikingly, unlike USH1 patients, none of the Ush1 mouse mutants display retinal degeneration (Libby and Steel, 2001; Ball et al., 2003; Johnson et al., 2003; Libby et al., 2003; Haywood-Watson et al., 2006; Ahmed et al., 2008; Williams et al., 2009; Lentz et al., 2010). A moderate increase of opsin concentration has been found in the connecting cilia of photoreceptors in a myosin VIIa–defective mouse mutant, suggesting a defect in the trafficking of this protein between the inner and outer segments of the photoreceptor cells (Liu et al., 1999). The only significant morphological difference between the retinas of Ush1 and wild-type mice is an aberrant positioning of the melanosomes and phagosomes in the retinal pigment epithelium cells of myosin VIIa–deficient mice (Liu et al., 1998; El-Amraoui et al., 2002; Gibbs et al., 2004). The consequence of this defect for retinal function is unknown. Remarkably, none of these abnormalities leads to retinitis pigmentosa and retinal degeneration, even in aged mutant mice (Libby and Steel, 2001; Ball et al., 2003; Libby et al., 2003; Haywood-Watson et al., 2006; Ahmed et al., 2008; Williams et al., 2009). This discrepancy between the mouse and human retinal phenotypes has made it particularly difficult to elucidate the roles of USH1 proteins in the human retina. This knowledge is now urgently required because, in the absence of animal models for the USH1 visual defect, the gene therapy strategies currently being developed cannot be guided by an understanding of the defective cell functions and molecular mechanisms that need to be restored.

We addressed this issue here. We considered that retinitis pigmentosa likely results from a common defective pathway for all the different USH1 genetic forms because it is not possible to distinguish between these forms in terms of the clinical presentation of the retinitis pigmentosa. Consistent with this idea, the pathogenesis of USH1 hearing impairment was elucidated by looking for holistic pathogenic explanations for deafness in the various USH1 genetic forms, which are also clinically indistinguishable in terms of hearing defect phenotype (El-Amraoui and Petit, 2005; Petit and Richardson, 2009; Richardson et al., 2011). USH1 proteins are present in different cochlear cell types, in both hair cells and nonsensory cells, and in various subcellular compartments in the hair cells, but the hair bundle has been shown to be the only structure containing all five interacting USH1 proteins (Boëda et al., 2002; Lefèvre et al., 2008; Caberlotto et al., 2011; Bonnet and El-Amraoui, 2012). Furthermore, we considered that the absence of retinitis pigmentosa in USH1 mouse mutants might enlighten the roles of USH1 proteins in the retinal degeneration observed in humans if the distribution of USH1 proteins differs significantly between mouse and human retinas: such differences could indeed account for the absence and presence of retinitis pigmentosa in mouse and man, respectively.

We provide here evidence for the existence of major differences between rodents and primates in the structural and molecular architecture of photoreceptor cells at the interface of the inner and outer segments, and for a differential distribution of USH1 proteins associated with this particular region. Our results strongly suggest that the retinal dystrophy observed in USH1 patients results from the failure of a previously unrecognized USH1 protein network involved in membrane–membrane coupling between the outer segment of the photoreceptors and the surrounding subcellular compartments.

## Results

### Low abundance of USH1 proteins in the mouse retina

We first analyzed the expression of the USH1 genes in the mouse retinal pigment epithelium and neural retina by RT-PCR (see Materials and methods). Only myosin VIIa transcripts were detected in the retinal pigment epithelium cells, whereas the transcripts of all five USH1 genes were present in the neural retina (Fig. 1 A). A similar expression pattern was found in human and macaque retinas (Fig. 1 A). Affymetrix array (GeneChip mouse genome 430 2.0 array) analyses of mouse retina mRNAs showed that *Myo7a* and *Pcdh15* transcripts were the only USH1 transcripts present in significant amounts. Their expression level was, however, about half that of transcripts derived from the genes defective in another type of USH syndrome, USH2—*Usherin* (*Ush2a*; Eudy et al., 1998), *Vlgr1/Gpr98 (Ush2c*; Weston et al., 2004), and *Whrn* (*Ush2d*; Ebermann et al., 2007; Fig. 1 B). This weak expression of USH1 genes in the murine neural retina was confirmed by RT-quantitative PCR (RT-qPCR) analysis in P15 mice (unpublished data). Comparative RT-qPCR analysis of USH1 transcripts in the neuroretinas of wild-type mice and *rd1* mutant mice that display an almost complete degeneration of the rods at P21 due to the lack of the rod-specific cGMP phosphodiesterase 6 (PDE6-β; Bowes et al., 1990) established an unambiguous expression by rod cells only for *Myo7a* and *Pcdh15* (Fig. 1 C).

To proceed with an in-depth and faithful analysis of the distribution of USH1 proteins, we generated six new rabbit polyclonal antibodies directed against murine USH1 proteins (Fig. 2 A; Materials and methods), which we used in this study in conjunction with previously reported anti-USH1 proteins antibodies. The specificity of all these antibodies was established on the cochlea of P3-P5 mice (Fig. 2 B) by the absence of hair bundle immunoreactivity in the USH1 mutant mice defective for the gene encoding the corresponding protein (Fig. S1 B). We then performed confocal microscopy analyses of the distribution of the five USH1 proteins on cryosections of adult mouse retinas (Fig. 2 C). Myosin VIIa was detected in both retinal pigment epithelium cells and photoreceptor cells (Fig. 2 C), in agreement with previous findings (Hasson et al., 1995; El-Amraoui et al., 1996; Liu et al., 1997). Myosin VIIa, sans, and faint protocadherin-15 stainings were observed in the inner segment of the photoreceptor (Fig. 2 C and unpublished data). By contrast, no specific immunostainings for the other two USH1 proteins, harmonin and cadherin-23, were detected in the mouse retina, whatever the conditions used for tissue fixation (Fig. 2 C and unpublished data).

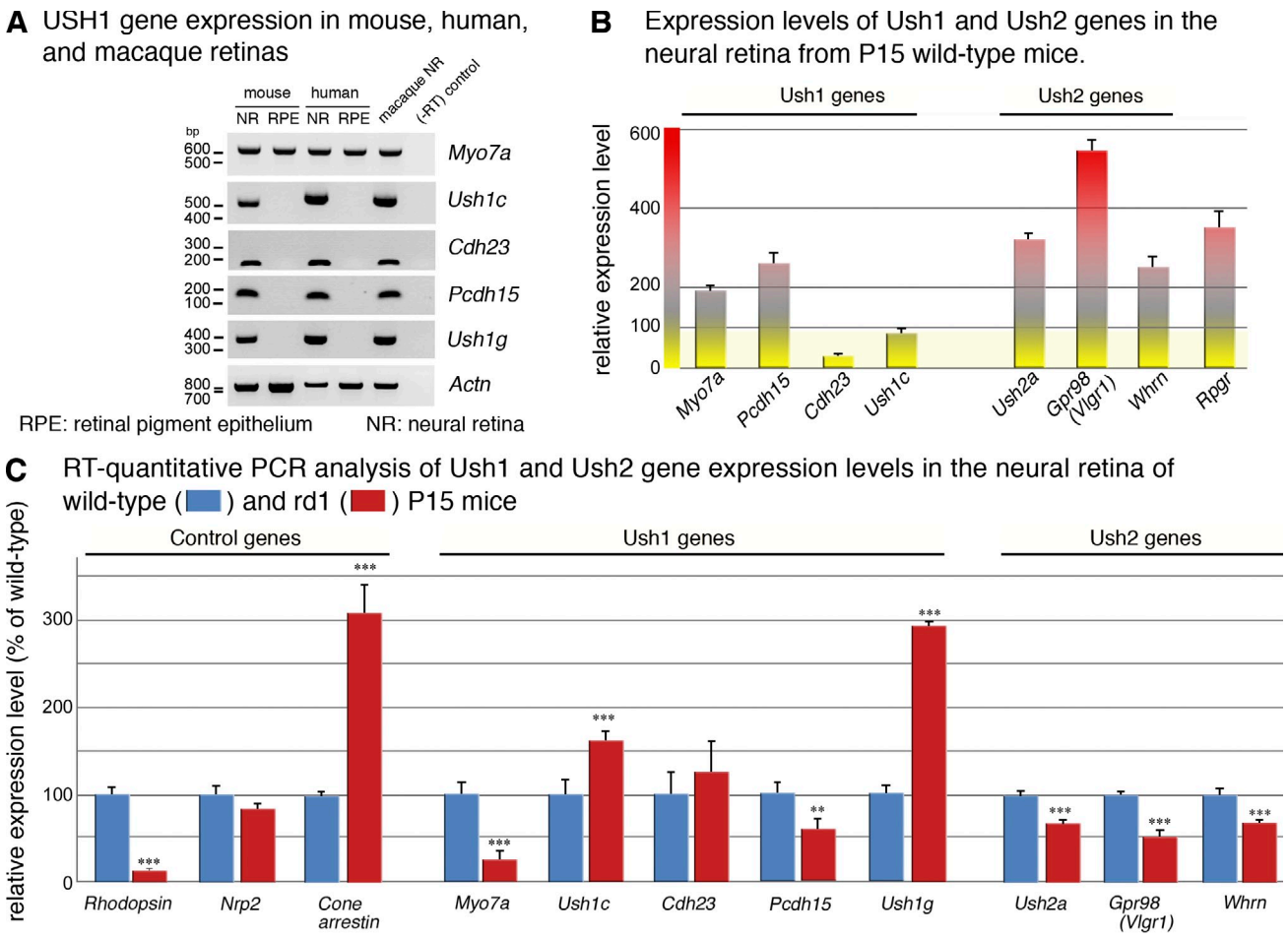


Figure 1. **USH1 transcripts in the murine retina.** (A) RT-PCR analysis of USH1 gene expression in the neural retina (NR) and the retinal pigment epithelium cells (RPE) of mice, humans, and macaques. In each case, a negative control without reverse transcription (−RT) was performed. (B) Transcriptomic analysis of USH1 and USH2 gene expression levels in the neural retina of wild-type mice. Note that sans transcripts are absent from the Affymetrix gene chips, and the relative levels of *Cdh23* and *Ush1c* transcripts are much lower than those of other USH1 and USH2 gene transcripts. (C) Quantitative RT-PCR analysis of the relative levels of USH1 and USH2 gene transcript expression in the neural retinas of wild-type and *rd1* P15 mice. The significantly lower abundance of the *Myo7a* and *Pcdh15, Ush2a, Gpr98* and *Whrn* transcripts in the retinas of *rd1* P15 mice indicates that the corresponding genes are expressed in mouse rod photoreceptors. **, $P < 0.01$; ***, $P < 0.001$ in Student's *t* test.

### The distributions of USH1 but not of USH2 proteins differ in mouse and macaque photoreceptor cells

We then investigated USH1 protein distribution in the retina of nonhuman primates. Immunostaining of cynomolgus monkey (*Macaca fascicularis*) retinas revealed strong staining for all five USH1 proteins in both rod and cone photoreceptors. All the USH1 proteins were detected in the region of the junction between the inner and outer segments (Fig. 2, D and E; and unpublished data).

This difference in USH1 protein distribution between mouse and macaque retinas led us to extend our interspecies comparison to USH2 proteins (Fig. 3, A and B; Fig. S1 C). Unlike USH1 proteins, USH2 proteins were readily detected in the mouse retina (Fig. 3 B; Materials and methods). Moreover, in both mouse and macaque retinas, usherin, Vlgr1, and whirlin were located at the junction between the inner and outer segments of the rod and cone photoreceptors, around the base of the connecting cilium, in the periciliary membrane complex region (Fig. 3 B).

Some USH1 or USH2 proteins were detected at other locations (e.g., in the synaptic region; unpublished data), but the inner–outer segment junctional region and the periciliary region of the photoreceptor cell were the only subcellular compartments in macaque retina that are associated to all the USH1 and USH2 proteins, respectively.

### Calyceal processes enclose the base of the outer segment in macaque but not in mouse photoreceptor cells

Given the detected difference in the distribution of USH1 proteins between the photoreceptors of mice and macaques, we undertook a comparative ultrastructural analysis of the inner–outer segment region in mouse and macaque photoreceptors (Fig. 4, A–D). Scanning electron microscopy analysis of the apical region of the inner segment showed the presence in macaques, but not in mice, of axially oriented microvillus-like structures, the calyceal processes, which form a collar around the base of the outer segment in both rod and cone photoreceptors (Fig. 4, A–D). Cones harbored 14–16 calyceal processes per cell, which were uniform in length (3 ± 0.06 µm), regularly spaced, extending parallel one to another, and tapering from base to tip

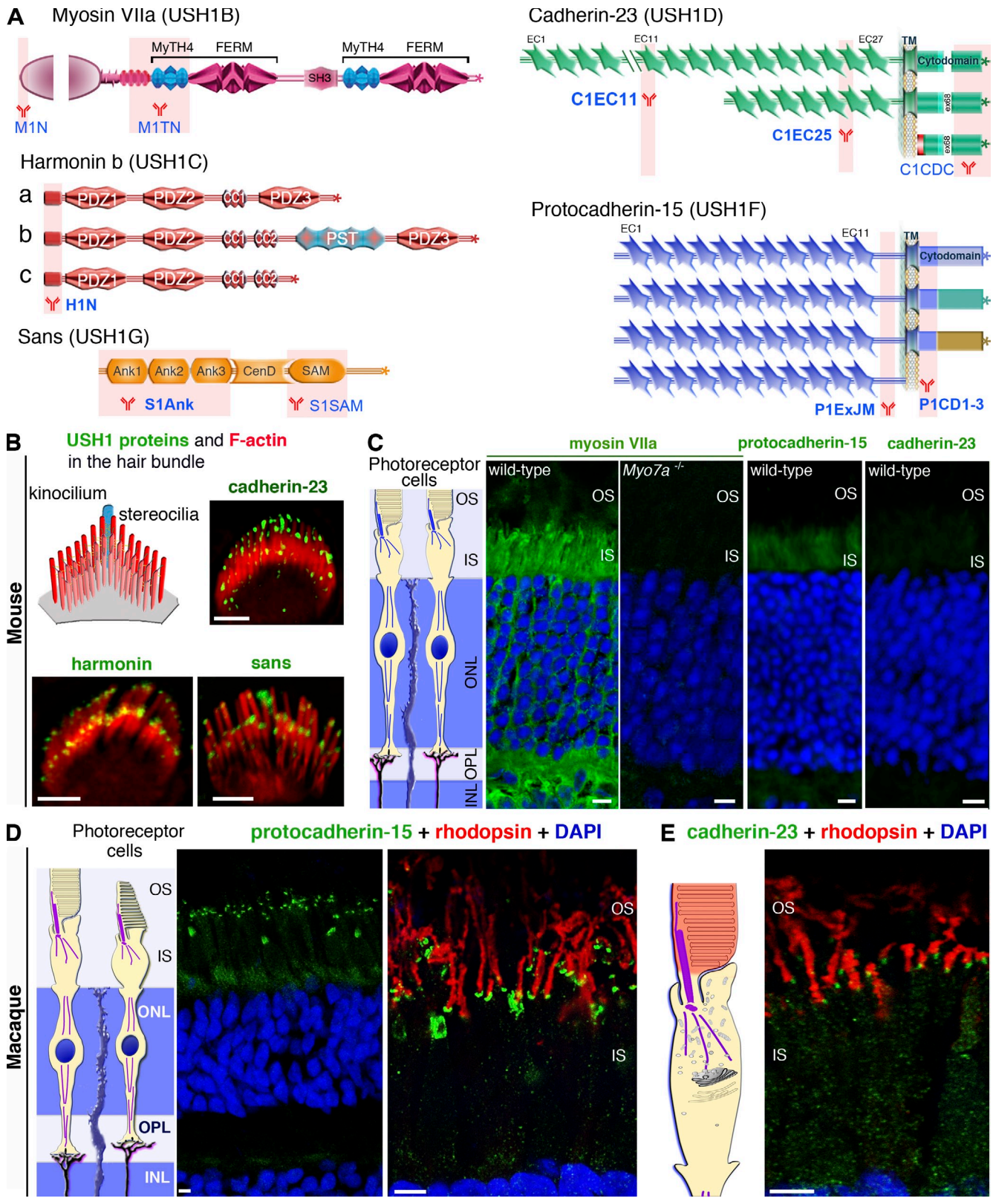


Figure 2. **USH1 proteins in mouse and macaque photoreceptors.** (A) Predicted structures of the USH1 proteins. The positions of the immunizing peptides and recombinant proteins used to engineer the new (in bold) and previously reported antibodies, relative to the different USH1 proteins isoforms, are indicated. (B and C) USH1 proteins in the murine inner ear and retina. (B) In the hair cells from cochleas of P3-P5 mice, cadherin-23, harmonin, and sans punctate immunostainings are detected at the tips of the stereocilia. (C) The organization of the outer neural retina is shown on the left. Myosin VIIa is detected in the inner segment (IS) of photoreceptors in wild-type but not in *Myo7a*$^{-/-}$ mice. By contrast, no significant cadherin-23 immunolabeling is detected in the mouse retina. (D and E) USH1 proteins in the macaque retina. Prominent immunostainings for protocadherin-15 and cadherin-23 are observed at the junction between the inner and outer (OS) segments of rod and cone photoreceptors. DAPI nuclear staining (blue) delineates the outer nuclear layer (ONL) and inner nuclear layer (INL). OPL, outer plexiform layer. Bars: (B) 2 µm; (C) 20 µm; (D, left) 10 µm; (D [right] and E) 5 µm.

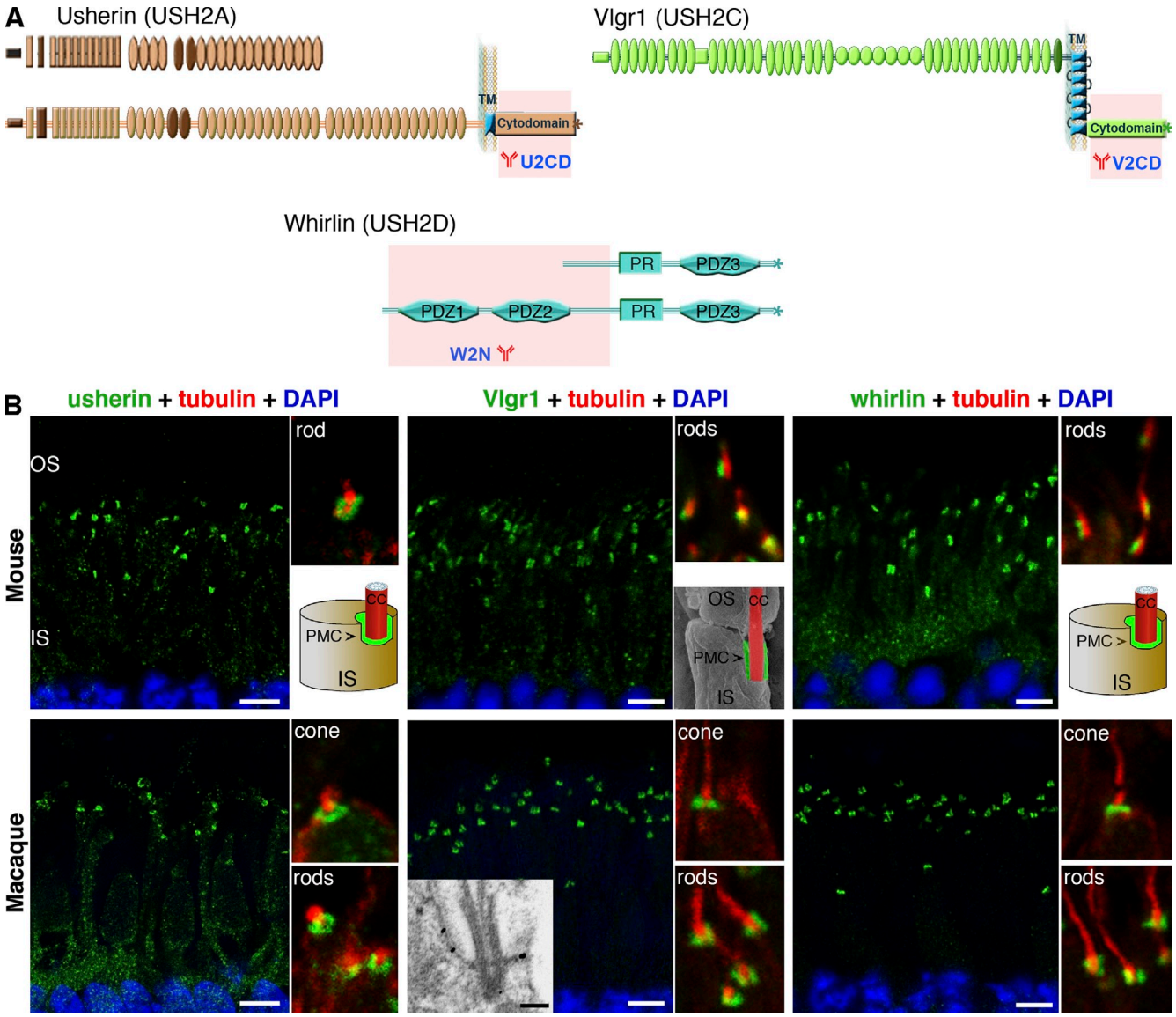


Figure 3. **USH2 proteins in mouse and macaque photoreceptors.** (A) Predicted structures of USH2 proteins. The positions of the recombinant proteins used to engineer the new antibodies (in bold) are indicated. (B) In both the mouse (top panels) and macaque (bottom panels) photoreceptors, usherin, Vlgr1, and whirlin are detected (green) in the periciliary membrane complex (PMC) region, around the connecting cilium (CC, highlighted in red in the schematic diagram). The inset in B (middle) shows immunogold labeling of Vlgr1 in the PMC region. Cell nuclei are stained with DAPI (blue). IS, inner segment; OS, outer segment. Bars: 5 µm; (B, inset) 250 nm.

(244 ± 5 nm diameter at the base and 144 ± 3 nm at the tip). The plasma membranes of the neighboring processes were 155 ± 12 nm apart at their bases and 180 ± 11 nm apart at their tips (Fig. 4 E). Together, these microvilli formed a uniform array around the basal fifth of the outer segment (Fig. 4, B–D). The array of calyceal processes appeared to be less regular in rods than in cones. They were fewer in number (~10 per cell), shorter (1.8 ± 0.12 µm), more variable in length (very long processes, 10–15 µm in length, were occasionally observed), and thinner (150 ± 10 nm at the base and 90 ± 3 nm at the tip) than in cones, and the distances between them were larger (220 ± 21 nm at the base and 295 ± 29 nm at the tip; Fig. 4 E).

The calyceal processes were first described ~50 years ago (Brown et al., 1963; Cohen, 1963), and have since been little studied. These microvilli are filled with uniformly polarized actin filaments, the barbed ends of which (plus ends) are located at their apical tips (O'Connor and Burnside, 1981). The phalloidin labeling of cones in macaques showed that the actin filament bundles of the calyceal processes extended farther down into the inner segment, over more than half its entire length, forming thick F-actin roots lying just beneath the plasma membrane (Fig. 4 G, arrowheads). The F-actin bundles of the calyceal processes and their roots were thinner in rods (Fig. 4 F).

No typical calyceal processes were detected in the mouse retina, in either rod or cone photoreceptors, at any of the stages analyzed (P30, P60, and 1-yr-old mice) and whatever the experimental conditions of tissue fixation (Fig. 4 A; Fig. S2 A). In either mouse or rat retinas, only occasionally did we observe rare, irregular membrane extensions, emerging from the

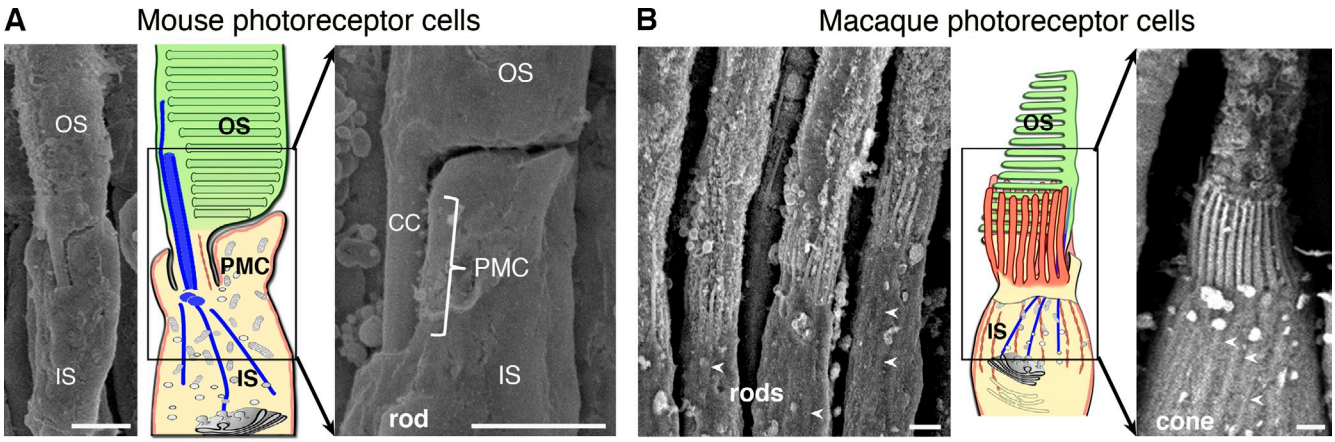


Macaque rod and cone photoreceptor cell calyceal processes

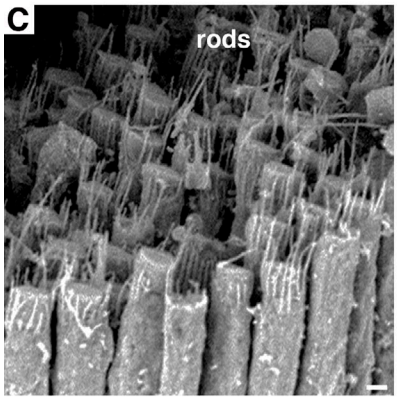


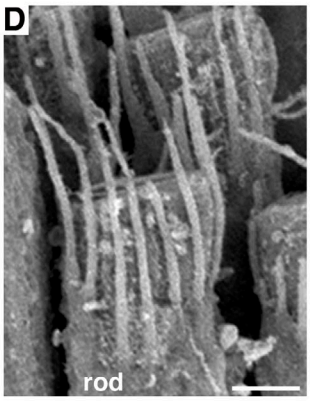


E

| | Cones (n=20, 182 CPs) | Rods (n=20, 96 CPs) |
|---|---|---|
| Number of calyceal processes (CPs) per photoreceptor | 14-16 | 10 |
| Length of CPs (number of CPs) | 3 ± 0.06 μm (152) | 1.8 ± 0.12 μm (74) |
| Diameter of CPs at the base | 244 ± 5 nm (91) | 150 ± 10 nm (52) |
| Diameter of CPs at the tip | 144 ± 3 nm (91) | 90 ± 3 nm (52) |
| Distance between CPs at their bases | 155 ±12 nm (60) | 220 ± 21 nm (36) |
| Distance between CPs at their tips | 180 ± 11 nm (60) | 295 ± 29 nm (52) |

Macaque photoreceptor cells

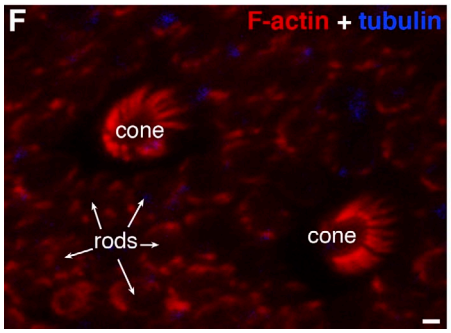


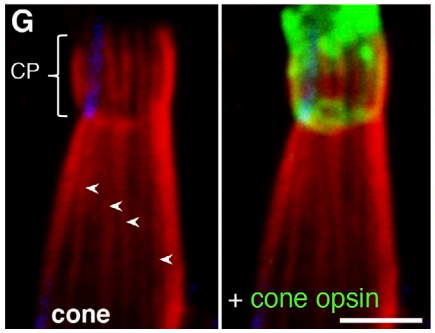


Human photoreceptor cells

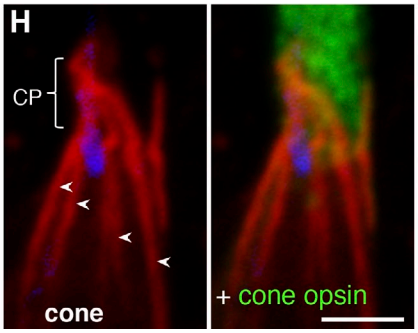


Figure 4. **Scanning electron microscopy analysis of the inner–outer segment interface in mouse and macaque photoreceptors.** (A) Mouse retina (perfused animals). The connecting cilium (CC), which connects the inner segment (IS) and outer segment (OS) of photoreceptors, and the periciliary membrane complex (PMC) region are visible. (B–G) Macaque retina (perfused animals). Finger-like structures, the calyceal processes (CP), protrude from the apical region of the inner segment, and surround the base of the outer segment. The absence (A, in mouse) or presence (B, in macaque) of the calyceal processes is highlighted in the schematic diagrams illustrating the structural features of a mouse rod (A) and macaque cone (B) photoreceptors. (C and D) Macaque photoreceptors with outer segments broken at the base display numerous calyceal processes, crowning the apical region of the remaining inner segment. (E) Measurement of calyceal processes in rod and cone photoreceptors (values are presented as mean ± SEM). The cone cells have larger numbers of thicker and more regularly spaced calyceal processes than the rod cells. (F and G) Flat-mount (F) and longitudinal cross-section (G) views of phalloidin-stained macaque retinas (perfused animals) show the calyceal processes containing actin filament bundles, with their roots extending downward into the inner segment (arrowheads). (H) Longitudinal cross-section of a phalloidin-stained human retina, illustrating the presence of the F-actin–labeled calyceal processes and their roots (arrowheads) in the apical region of the inner segment of a cone photoreceptor cell. Bars: (A–D) 1 μm; (F–H) 2 μm.

upper edge of the inner segment and projecting on the base of the outer segment in cone cells, here referred to as vestigial calyceal processes (Fig. S2 B). Consistently, mouse and rat photoreceptors also lacked F-actin bundles extending both around the base of the outer segment or into the inner segment (Fig. 4 G; Fig. S2, A–C).

### USH1 proteins are located at the calyceal processes of macaque and human photoreceptors

Immunostaining for myosin VIIa, harmonin, cadherin-23, protocadherin-15, and sans, analyzed by high-resolution confocal microscopy on flat-mounted macaque retinas, revealed regularly

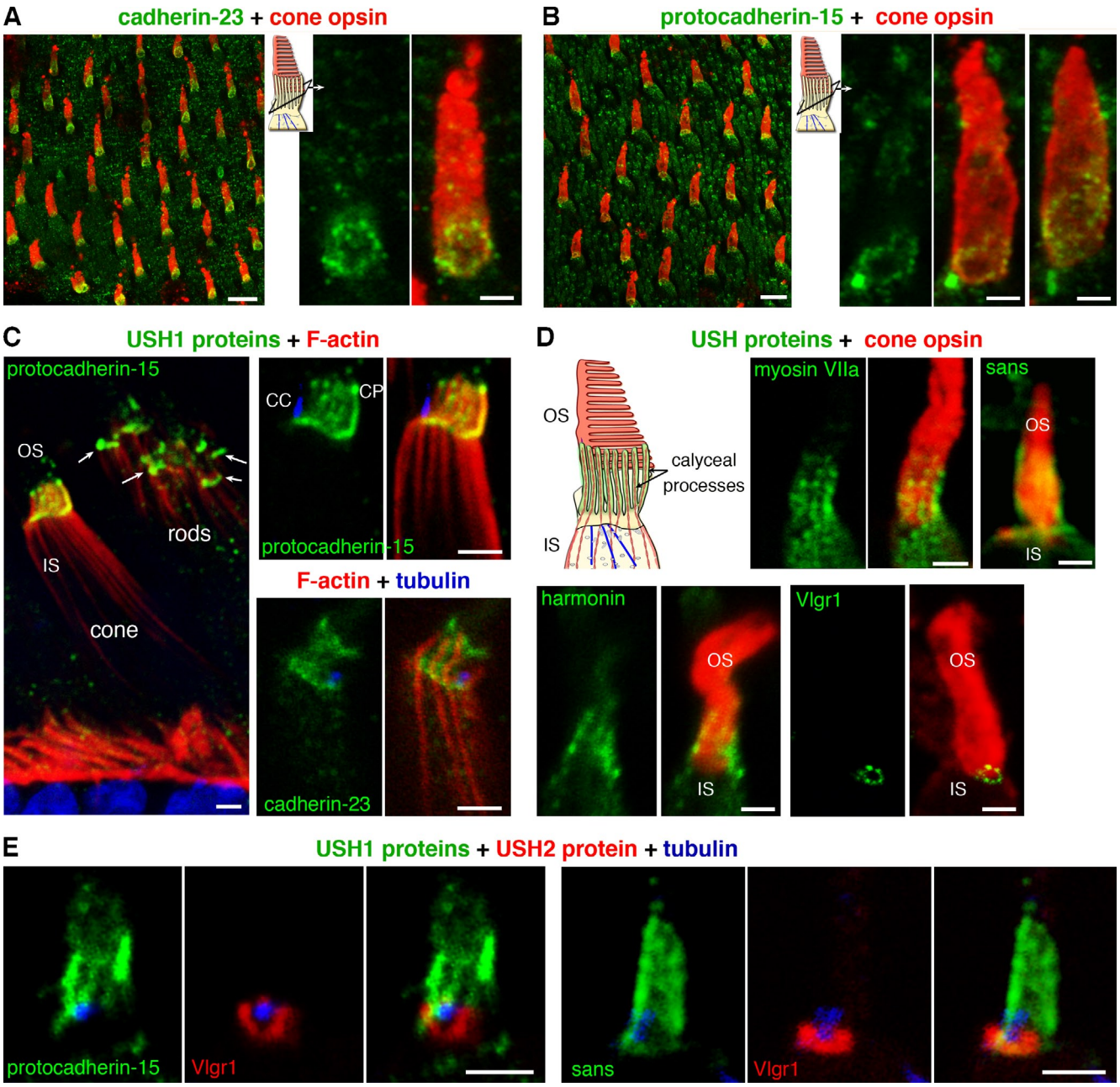


Figure 5. **USH1 and USH2 proteins are located in different compartments of the photoreceptors.** (A and B) Flat-mount retina. A single confocal z-section illustrating the immunostainings of cadherin-23 and protocadherin-15 (green) in the calyceal processes surrounding the proximal region of the outer segment. Cone labeling (red) from several confocal stacks was used to delineate the outer segment. (C and D) In longitudinal sections of the adult macaque retina, protocadherin-15 (C), cadherin-23 (C), myosin VIIa (D), sans (D), and harmonin (D), but not Vlgr1 (D), are detected along the calyceal processes. Note the intense protocadherin-15 labeling (green) at the inner–outer segment junction in rod photoreceptors (C, left panel, arrows). (D) Vlgr1 immunostaining is restricted to the periciliary membrane complex region, whereas the labeling for myosin VIIa, sans, and harmonin extend further, spreading along the calyceal processes surrounding the cone opsin-labeled outer segment. (E) Double-staining of protocadherin-15 and Vlgr1 (left panels), or sans and Vlgr1 (right panels), further confirms the location of USH1 and USH2 proteins in different subcellular compartments of the photoreceptor cell. Bars: (A and B, left panels) 10 µm; (A and B, right panel, and C–E) 2 µm.

spaced puncta (8–10 spots in rods and 14–16 in cones) detected in the immediate vicinity of the F-actin–labeled calyceal processes (Fig. 5, A–C, and Fig. 6 A). Analysis of retinal cryosections showed an additional intense USH1 labeling at the junction between the inner and outer segments in rods (Fig. 5 C, arrows; Fig. S3 A) but not in cones (Fig. 5, C and D). This distribution of USH1 proteins clearly differed from that of USH2 proteins, as demonstrated by double-labeling experiments for USH1 and USH2 proteins on macaque retinas, with usherin, Vlgr1, and whirlin being restricted to the periciliary membrane region (Fig. 3, B–D; Fig. 5, D and E).

We extended our analysis to human photoreceptors. Human photoreceptors displayed the F-actin–labeled calyceal processes' roots (Fig. 4 H), similar to those observed in macaque (Fig. 4 G; Fig. S2 C) or pig photoreceptors (Fig. S2 D). Scanning electron

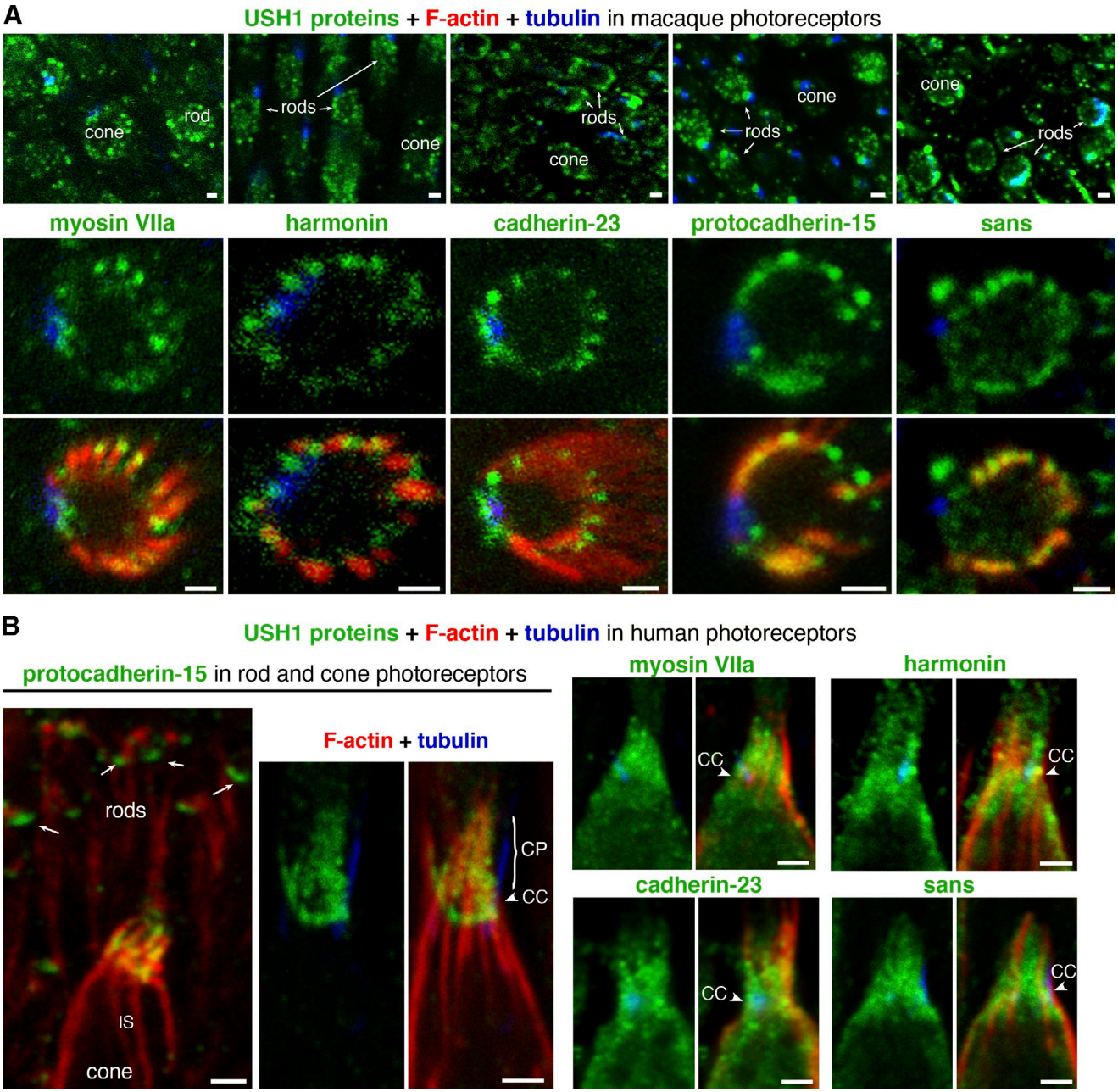


Figure 6. **USH1 proteins in the calyceal processes of macaque and human photoreceptors.** (A) Confocal cross-sections of rod (top panels), and cone (bottom panels) photoreceptors at the level of the connecting cilium (CC) from flat-mount macaque retinas. The five USH1 proteins—myosin VIIa, harmonin, cadherin-23, protocadherin-15, sans—display punctate patterns of staining around the base of the outer segment. The microfilament (F-actin) and microtubule (glutamylated tubulin) cytoskeletons are labeled in red and blue, respectively. (B) In longitudinal sections of a human retina, protocadherin-15 is detected along the calyceal processes (CP). Intense labeling is observed at the inner–outer segment junction in rod photoreceptors (arrows). Myosin VIIa, harmonin, cadherin-23, and sans also are detected along the calyceal processes. IS, inner segment. Bars, 2 µm.

microscopy and immunostaining experiments revealed that calyceal processes were preserved in only a few photoreceptors, often with reduced length (Fig. S4 A), in agreement with our observations that in macaque retinas these structures could be systematically observed only in perfused animals (Fig. S3, B and C, and Fig. S4 B). Nevertheless, when present, human calyceal processes also were associated with USH1 proteins (Fig. 6 B). Moreover, strong immunostaining of USH1 proteins was detected at the inner–outer segment junction of human rods (Fig. 6 B, left panel, arrows), as in macaque rods (Fig. 5 C, arrows).

Immunogold labeling using antibodies directed against the extracellular and intracellular epitopes of either cadherin-23 or protocadherin-15 revealed a high density of gold particles along the photoreceptor calyceal processes (Fig. 7, A–E). Protocadherin-15– and cadherin-23–specific gold particles were observed at the membranes of both the calyceal processes (Fig. 7, A, C, and E, black arrowheads) and the apposed edge of the outer segment (Fig. 7, A, C, and E, open arrowheads). Some gold particles were also detected between the calyceal processes themselves (Fig. 7, A and C; and unpublished data).

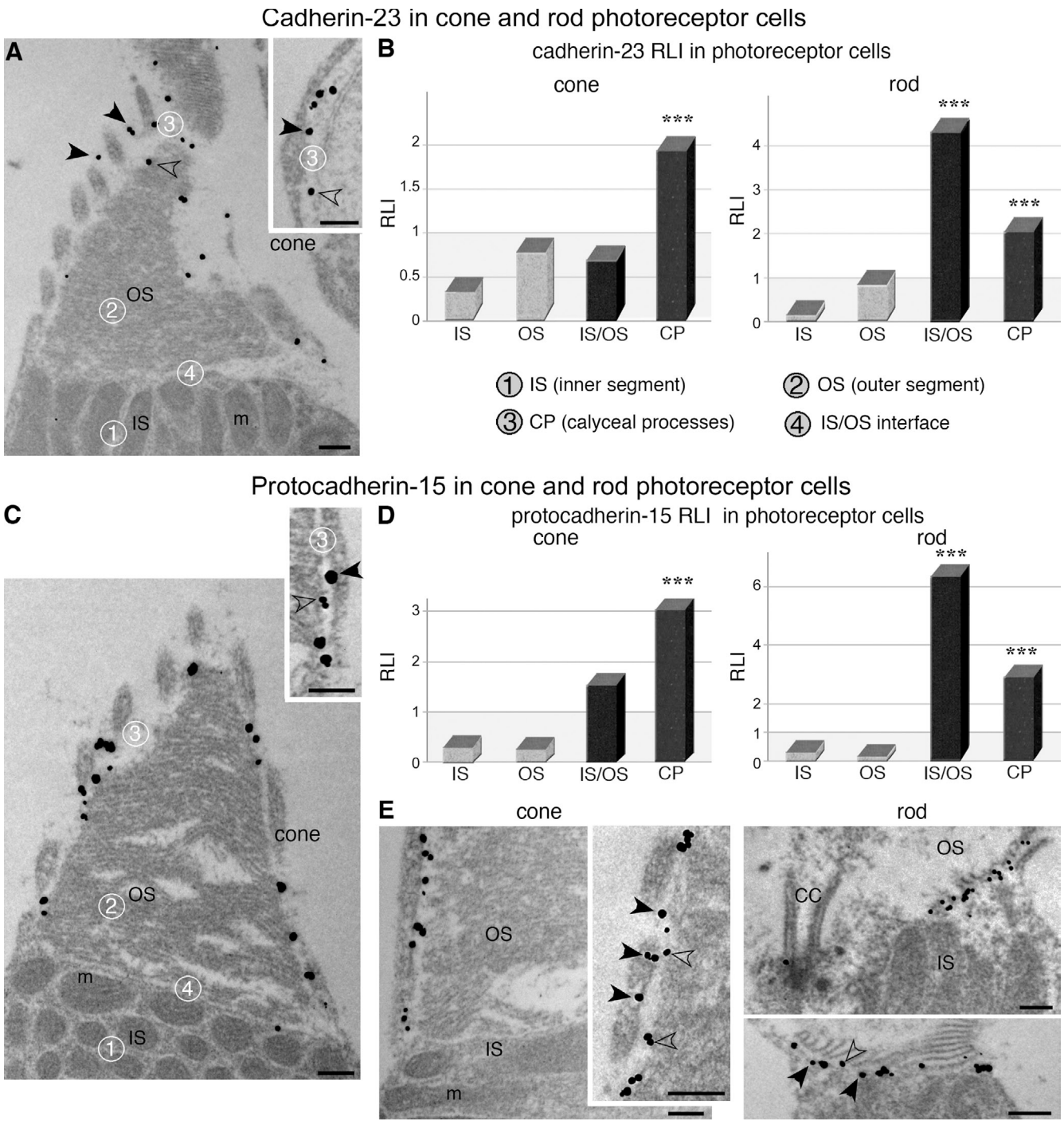


Figure 7. **Cadherin-23 and protocadherin-15 immunogold labelings in macaque photoreceptors.** The C1EC25 and P1CD1-3 antibodies were used to detect cadherin-23 and protocadherin-15, respectively. (A, C, and E) Cadherin-23 (A) and protocadherin-15 (C and E) silver-enhanced immunogold particles are present along the apposing membranes of the macaque photoreceptor outer segment and calyceal processes. Gold particles are detected on either side, both at the edge of the outer segment (empty arrowheads) and at the calyceal processes (filled arrowheads). Quantitative analyses of the immunogold labeling for cadherin-23 (B) and protocadherin-15 (D) were performed on nine photoreceptors, subdivided into four regions (1, 2, 3, 4), as indicated in A and C. Gold particle distributions are expressed as the relative labeling index (RLI). In all the photoreceptors examined, numerous gold particles are observed along the calyceal processes and at the inner–outer segment interface. Rod photoreceptors display larger numbers of gold particles at the inner–outer segment interface for both cadherin-23 and protocadherin-15 (B and D), as illustrated in E. In cone photoreceptors, however, gold particles associate essentially with the calyceal processes (A–E). m, mitochondria. ***, $P < 0.001$ in $\chi^2$ test. Bars, 250 nm.

Quantification and statistical analysis of cadherin-23 and protocadherin-15 nanogold labeling patterns in photoreceptor compartments showed that the calyceal processes were associated with twice (for cadherin-23) or three times (for protocadherin-15) the number of gold particles expected for a random distribution of these particles, as shown by determination of the relative labeling index (RLI, $P < 0.001$; Mayhew et al., 2009). Consistent with USH1 immunofluorescence labeling (Figs. 5 and 6),

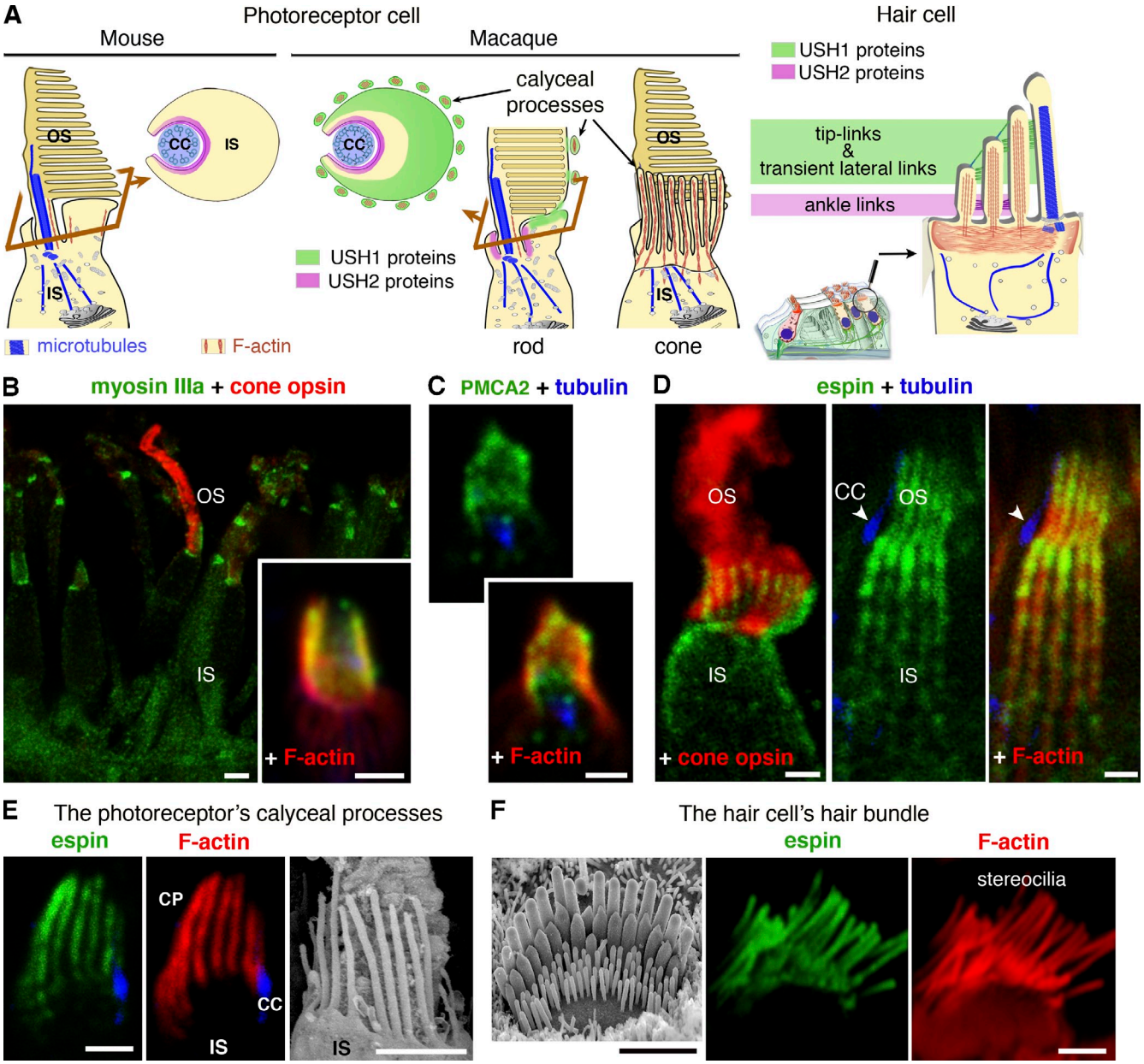


Figure 8. **Other proteins common to the calyceal processes of photoreceptors and the stereocilia of hair cells.** (A) Schematic diagrams illustrating the differences in architecture of the apical-most inner segment regions of mouse and macaque photoreceptors, and summarizing the subcellular distribution of USH1 and USH2 proteins. In the diagram of the rod cell, the calyceal processes are not presented, to visualize the distribution of USH1 proteins at the junction between inner and outer segments. The precise boundaries of the USH1 protein labeling in this region (green) remain to be established. (B–D) Myosin IIIa, PMCA2, and espin in the photoreceptor calyceal processes. Glutamylated tubulin (blue) and cone opsin (red) labeling was used to visualize the connecting cilium and the cone outer segment, respectively. (E and F) Espin labeling in the calyceal processes of a cone photoreceptor cell (E) and the hair bundle of an auditory hair cell (F). The scanning electron microscopy images show the architecture of the calyceal processes of a cone photoreceptor (E) and an auditory sensory cell's hair bundle (F). Bars, 2 µm.

a comparison of the distributions of protocadherin-15 and cadherin-23 in rods and cones showed that only rods ($P < 0.05$, Mann-Whitney test) had a significantly higher density of gold particles at the junction between the inner and outer segments than elsewhere. In this region, the numbers of protocadherin-15 and cadherin-23 particles were more than six and four times greater, respectively, than would be expected from a random distribution (Fig. 7, B and D).

The presence of the USH1 proteins along the calyceal processes led us to characterize these microvilli further (Fig. 8 A). We explored the possibility that calyceal processes and stereocilia have other molecular components in common. We investigated the presence of myosin IIIa (Fig. 8 B), the $Ca^{2+}$ pump PMCA2 (plasma membrane calcium-transporting ATPase 2; Fig. 8 C), and the F-actin cross-linker espin (Fig. 8 D). All three proteins were detected in the calyceal processes (Fig. 8, B–E). Espin immunostaining, whether detected with anti-pan espin or anti-espin 1 antibodies, extended several micrometers farther down the roots of the calyceal processes in the inner segment (Fig. 8 D; Fig. S3, B and C).

### The network of USH1 proteins at the basolateral region of the outer segment is conserved in frogs

Based on the pattern of USH1 proteins in the human and macaque neuroretinas, we investigated the possibility that this pattern was present in ancestral vertebrates, despite its absence in mouse and rat. We focused on frogs, because of the well-documented presence of calyceal processes in amphibian photoreceptor cells (Fig. 9, A–G; O'Connor and Burnside, 1981; Williams et al., 1988; Pagh-Roehl et al., 1992) and the possibility of carrying out retinal biochemistry analysis in these animals. In both *Xenopus laevis* and *Rana catesbeiana* (bullfrog), all five USH1 proteins, as well as myosin IIIa, espin, and PMCA2, were detected along the calyceal processes of rods and cones (Lin-Jones et al., 2004), as in macaque photoreceptors (Fig. 6 A). However, by contrast to what we observed for macaque calyceal processes, which shrink rapidly upon isolation of the neural retina (Fig. S3, B and C), frog calyceal processes and their F-actin–labeled roots remained stable for at least 2 h under the same experimental conditions (Fig. S4 C). The distribution of USH2 proteins was restricted, as in macaque and mouse photoreceptors, to the periciliary ridge region (Fig. 9 D).

Together, our data suggest that USH1 proteins might interact at the basolateral region of the outer segment. The in vitro interactions between USH1 proteins are well documented (Richardson et al., 2011; Pan and Zhang, 2012), but no biochemical evidence supporting the in vivo formation of an USH1 protein complex has yet been obtained. Here, we used two anti-sans antibodies, the S1Ank antibody directed against the N-terminal ankyrin domains and the S1SAM antibody directed against the C-terminal SAM domain (see Fig. 2 A), incubated with protein extracts from *Xenopus* retinas. Endogenous myosin VIIa and harmonin were coimmunoprecipitated with the S1Ank or S1SAM antibody, but not with protein G alone (Fig. 9 B). This indicates that bipartite sans–myosin VIIa and sans–harmonin complexes or tripartite sans–myosin VIIa–harmonin complexes form in the frog photoreceptor cells.

Cadherin-23 and protocadherin-15 have been shown to interact via their first extracellular repeats (EC1) to form fibrous links in the hair bundles of cochlear hair cells, which are insensitive to the protease subtilisin (Goodyear and Richardson, 2003) but sensitive to the $Ca^{2+}$ chelator BAPTA. Accordingly, when *Xenopus* retinas were treated with subtilisin and processed for scanning electron microscopy, no significant difference was found between the calyceal processes of treated and control retinas (Fig. 9 E). However, if the retina was treated with subtilisin and then with BAPTA, we observed, in almost every photoreceptor cell, the detachment of calyceal processes from their axial indentations of the outer segment, in which they would normally be embedded (Fig. 9 E).

### Calyceal processes ensheathing the emerging outer segment in *Xenopus* photoreceptor cells already express USH1 proteins

The observation of electroretinographic anomalies in USH1 patients during the early postnatal period suggests that USH1 proteins may be involved in photoreceptor morphogenesis during embryonic development. We thus switched to *Xenopus* to characterize the sequence of early morphological changes at the inner–outer segment region during the morphogenesis of photoreceptors, by electron microscopy (Fig. 10, and unpublished data). Up to stage 35, photoreceptors of *Xenopus* tadpoles' retinas were elongated cells with a developing inner segment but no outer segment (unpublished data). From stage 37–38 onwards, most of the photoreceptors had filopodium-like processes in the distal region of their inner segment that were developing calyceal processes (Fig. 10, A and D). These structures, which appear as non-rigid extensions, did not yet display detectable phalloidin labeling all along (Fig. 10, B and E). USH1 proteins were already detected in the distal region of the elongating inner segment at this stage, the labeling often being observed above the level of the connecting cilium (Fig. 10, B and C, and unpublished data). At stage 41–42, the calyceal processes had increased in length, and were usually of a similar height to the growing outer segment (Fig. 10 H, and unpublished data). The core of the actin filament bundles of the calyceal processes now was labeled along its entire length by phalloidin, and USH1 protein immunostaining colocalized with these actin filaments (Fig. 10 H). As development proceeded, the calyceal processes displayed increasingly intense USH1 immunostaining (Fig. 10 I, and unpublished data). Thus, calyceal processes, which emerge before the outer segment, contain the USH1 proteins as soon as they begin to enclose the growing outer segment.

## Discussion

In primates, the five USH1 proteins colocalize at membrane–membrane connection sites between the outer segment of the photoreceptors and surrounding subcellular compartments—the calyceal processes—in both rods and cones, and the inner segment in rods only. This finding raises the question of why USH1 proteins have previously escaped detection at these subcellular compartments. One reason is the focus of previous studies on mouse retina (Ahmed et al., 2003; Reiners et al., 2003, 2005; Reiners and Wolfrum, 2006; Maerker et al., 2008). As shown here, not only do mouse photoreceptors lack calyceal processes, but USH1 proteins are not detectable in the outer segment basal region of murine photoreceptors, even with recently generated antibodies that invariably and specifically labeled the USH1 proteins in the murine inner ear hair cells (Fig. 1, A and B; Fig. S1 C). Even more surprising is the previous lack of detection of the association of USH1 proteins with the calyceal processes revealed here, in previous studies of primate (human and macaque) neuroretinas (Liu et al., 1997; Ahmed et al., 2003; Lagziel et al., 2009). The most likely explanation is the extreme lability of the calyceal processes. These processes were systematically present in the retinas of perfused macaques or pigs, but were not preserved if retinas were harvested and post-fixed within 20 min, the standard conditions for tissue fixation (Fig. S3, B and C; Fig. S4 B). This lability of the calyceal processes is also a characteristic of human photoreceptors, as suggested by inconsistent results for their detection and their heterogeneity, in terms of numbers and length, in photoreceptors of human post-mortem retinal samples (Fig. S4 A).

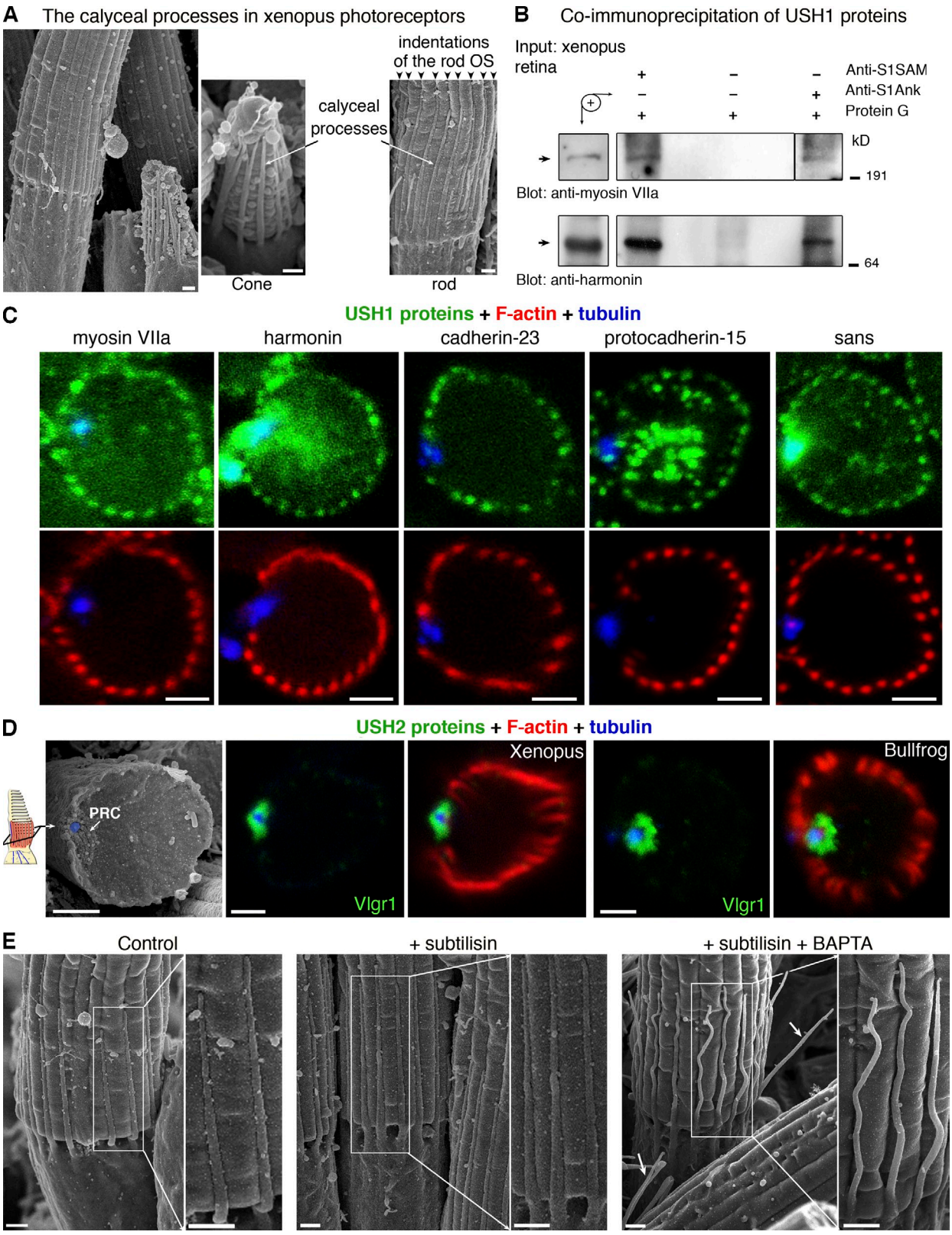


Figure 9. **USH1 and USH2 proteins in the calyceal processes of adult amphibian photoreceptors.** (A) Adult *Xenopus laevis* photoreceptors. Multiple indentations run along the photoreceptor outer segment (OS) from its base to its tip. These indentations are occupied at their base by well-developed calyceal processes (CP). (B) Co-immunoprecipitation of USH1 proteins. Using adult *Xenopus* retinal extracts, the anti-sans antibodies anti-S1SAM and anti-S1Ank, but not protein G alone, immunoprecipitate endogenous myosin VIIa (top panels) and harmonin (bottom panels). (C and D) Flat-mount sections of *Xenopus* and bullfrog photoreceptors. The USH1 proteins are detected nearby the F-actin–labeled (red) calyceal processes (C), whereas the USH2 protein Vlgr1 is restricted to the periciliary ridge complex (PRC) region surrounding the labeled connecting cilium (blue immunolabeling, highlighted on the scanning electron micrograph of a broken rod). (E) Retinas from adult *Xenopus* ($n$ = 3) were incubated in Ringer solution alone, or containing subtilisin, or subtilisin

Our results highlight the existence of marked interspecies difference(s) in the photoreceptor outer–inner segment relationship. They show that the basal fifth of the outer segment and the apical half of the inner segment should be regarded as framed together within a continuous F-actin cytoskeletal girdle. Indeed, in human, macaque, pig, and frog photoreceptors, the F-actin core of the calyceal processes extends large F-actin bundles that penetrate downward, beneath the plasma membrane of the apical half of the inner segment (Fig. 4, G and H; Fig. S2). These calyceal process roots, absent in mouse and rat photoreceptors (Fig. S2 B), are the stable landmarks of the labile calyceal processes. The presence of several F-actin cross-linking proteins—fimbrins/plastins (Höfer and Drenckhahn, 1993), fascin 2 (Lin-Jones and Burnside, 2007), and espin (this paper)—in the calyceal processes indicates that they are rigid microvilli.

The five USH1 proteins have been shown to interact in vitro (Boëda et al., 2002; Siemens et al., 2002; Weil et al., 2003; Adato et al., 2005; Pan et al., 2009; Bahloul et al., 2010; El-Amraoui and Petit, 2010; Yan et al., 2010; Caberlotto et al., 2011; Richardson et al., 2011; Wu et al., 2011; Pan and Zhang, 2012). Cadherin-23 and protocadherin-15 form heteromeric structures that can be observed as fibrous links within the hair bundles, specifically, the transient lateral links (Petit, 2001; Boëda et al., 2002; Adato et al., 2005; Lagziel et al., 2005; Michel et al., 2005), and the tip-link (Kazmierczak et al., 2007). The other three USH1 proteins, harmonin, sans, and myosin VIIa, anchor these links to the actin filaments of the stereocilia (Fig. 8 A, Fig. S1 A; Boëda et al., 2002; Siemens et al., 2002; Weil et al., 2003; Grillet et al., 2009; Michalski et al., 2009; Caberlotto et al., 2011; Grati and Kachar, 2011). The immunoprecipitation experiments demonstrated for the first time the existence of an USH1 protein complex containing all three USH1 proteins in vivo. Furthermore, both the largest isoform of cadherin-23 (detected with the C1EC11 antibody) and protocadherin-15, which interact via their N-terminal EC1 repeats (Kazmierczak et al., 2007; Sotomayor et al., 2010), were found to be present at membrane interfaces between the outer segment and surrounding calyceal processes, and between the base of the outer segment and the apical region of the inner segment. They are thus predicted to form heteromeric adhesion bridges at these sites. The USH1 protein complex is therefore qualified to form an adhesion belt connecting the outer segment basal region to the surrounding structures. The detachment of the calyceal processes along their entire length after treatment with BAPTA (Fig. 9, F–H) in the frog is consistent with the USH1 proteins playing a key role in the connection of the calyceal processes to the outer segment, although this does not rule out a role for other adhesion proteins with similar characteristics. Cadherin-23– and protocadherin-15–specific gold particles were also detected between adjacent calyceal processes (Fig. 7 and unpublished data). In the well-ordered crown-like structure at the base of the cone outer segments, the calyceal processes are ∼150 nm (at their base) to 180 nm (at their tip region) apart (Fig. 4 E). This distance, which is similar to that spanned by the tip-links (∼150 nm long, from 90 nm to 190 nm; Furness et al., 2008), is thus consistent with the existence of cadherin-23–protocadherin-15 links between the calyceal processes.

The conservation of USH1 protein distribution in the calyceal processes between frogs and humans, which are evolutionary distant of ∼300 million years, strongly argues for a pivotal role of the USH1 protein network in this structure. Furthermore, the presence of PMCA2, the fastest known neuronal $Ca^{2+}$ pump (Caride et al., 2001), in both frog and macaque calyceal processes, highlights the importance of active $Ca^{2+}$ ion extrusion from this compartment, which is thus expected to control the strength and rigidity of a $Ca^{2+}$-dependent adhesion bridge formed by the two cadherins between the calyceal processes and the outer segment (Elledge et al., 2010; Sotomayor et al., 2010; Giacomello et al., 2011). The $Ca^{2+}$ concentration within the calyceal processes, by regulating myosin VIIa motor activity, is predicted to control the tension forces generated by this motor protein (Inoue and Ikebe, 2003; Henn and De La Cruz, 2005; Heissler and Manstein, 2012). The USH1 protein adhesion network of photoreceptors would therefore act as a mechanical device producing, conveying, and possibly probing tension forces.

Our results, showing a difference in the distribution of USH1 proteins in the photoreceptors of primates (humans and nonhuman primates) and rodents, which display and do not display retinal degeneration, respectively, when USH1 proteins are defective, strongly support evidence for the presence/absence of calyceal processes as being the cause of this difference in phenotype between humans and mice. So, what role does the USH1 protein-mediated adhesion complex play? USH1 proteins are present not only along the calyceal processes of the mature photoreceptors, but also during outer segment growth in *Xenopus* tadpoles and in early postnatal macaque photoreceptors. By cupping the base of the outer segment, in which the nascent outer disks fold, first during embryogenesis and then throughout life, to ensure the daily renewal of photoreceptor outer segments (Steinberg et al., 1980; Eckmiller, 1987; Kennedy and Malicki, 2009; Sung and Chuang, 2010), the USH1 protein network may be involved in both the formation and maintenance of the outer disks, the site of visual phototransduction. By affecting the adhesion of the calyceal processes to the outer segment, the absence of the USH1 protein network may in addition alter the F-actin roots of these processes, thereby modifying the cytoarchitecture of the inner segment. The presence of the USH1 proteins at the outer–inner segment interface in macaque rods gives additional support to a role for this complex in outer disk biogenesis. The high abundance of this complex at this site in rods and its low abundance in cones further argue in favor of such a role, as outer disk/lamella formation differs between the two types of photoreceptors. In rod outer

followed by BAPTA. Subtilisin treatment did not affect the attachment of the calyceal processes to the outer segment, but the addition of BAPTA resulted in the detachment of the calyceal processes, which lost their connection to the plasma membrane of the outer segment, sometimes along their entire length (arrows). Bars: (A and E) 1 µm; (C and D) 2 µm.

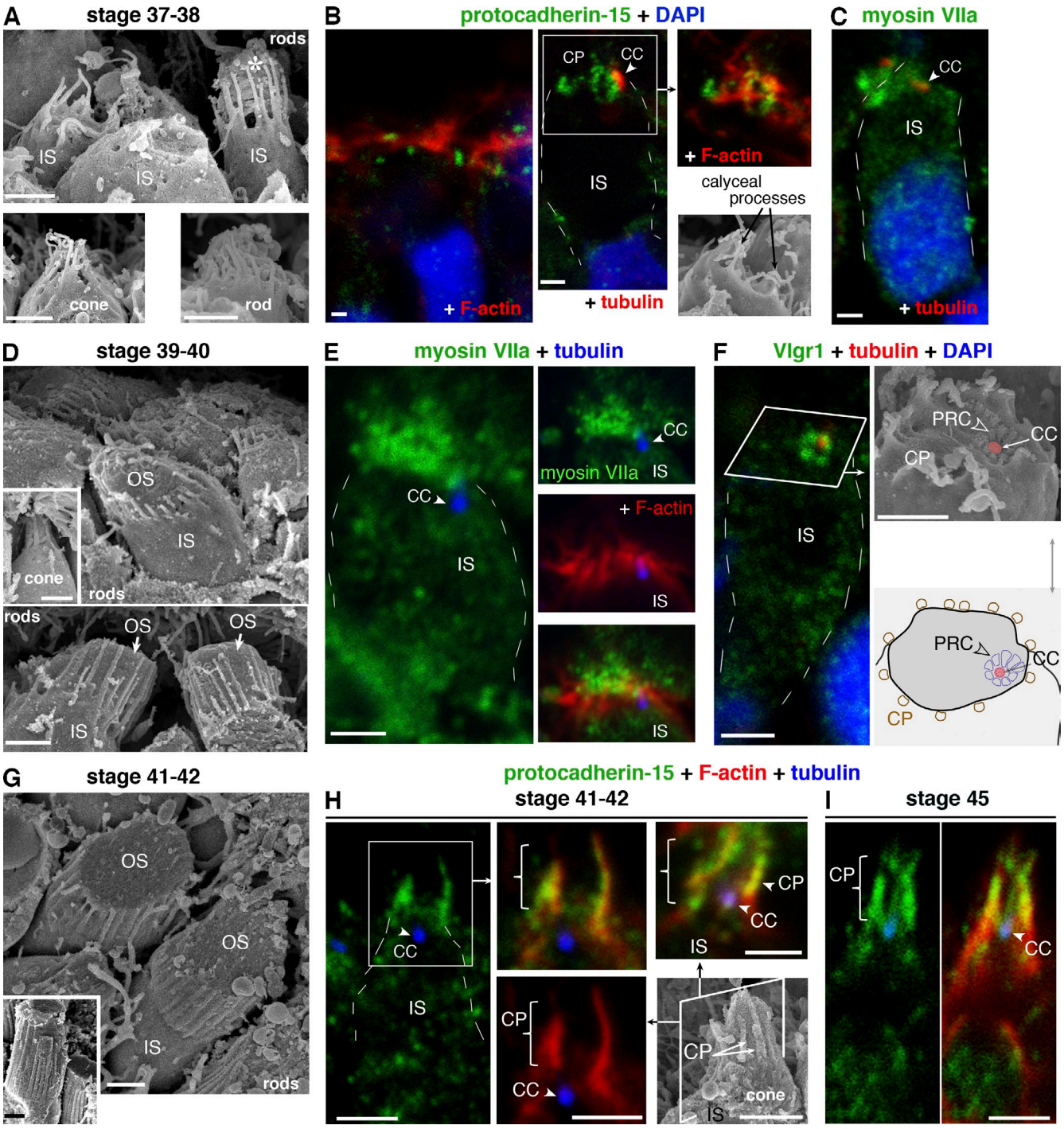


Figure 10. **USH1 and USH2 proteins in developing photoreceptors in *Xenopus laevis*.** (A–I) Scanning electron microscopy (left panels) and confocal microscopy analysis of USH protein immunolabeling at various stages of *Xenopus* development. (A–C) At stage 37–38, a few photoreceptors display developing calyceal processes (CP) that protrude from the distal region of the inner segment (IS) (A). Occasionally, a more developed outer segment with a basket of calyceal processes is observed (A, asterisk). Immunostaining for protocadherin-15 (B) and myosin VIIa (C) is detected in the distal region of the inner segment, at about the level at which the connecting cilium (CC) develops. (D–F) At stage 39–40, well-delimited calyceal processes surround the growing outer segments (D). At this stage, multiple myosin VIIa–immunoreactive spots are observed above the connecting cilium and at the tip of the inner segment, which is visualized by F-actin labeling (E). The USH2 protein Vlgr1 is detected in the periciliary ridge complex (PRC) region (F). (G and H) At stage 41–42, well developed calyceal processes are observed in almost all the photoreceptors (G). The protocadherin-15 staining coincides with the presence of the calyceal processes, which are visualized by F-actin immunostaining (red), at both stage 40–41 (H) and stage 45 (I). Bars, 2 µm.

segments, closely apposed disks are pinched off from the evaginated membranes and are surrounded by the outer segment external plasma membrane, whereas in cone outer segments, simple evaginations of the plasma membrane form outer disk lamellae exposed to the extracellular environment (Eckmiller, 1987; Kennedy and Malicki, 2009). Future studies directly probing the role of the calyceal processes may shed light on the reasons for their dispensability in some vertebrate species.

A structural role of the calyceal processes has been suggested, increasing the rigidity of the inner–outer segment junction important for the formation of photoreceptor outer disks. A higher density of the photoreceptor cells or an association with a more rigid surrounding extracellular matrix may compensate for the absence of well-developed calyceal processes. In addition, a more specific function related to the vision process in diurnal animals should also be considered.

Our findings suggest that the frog model may be only partially informative and not necessarily the most appropriate animal model of the USH1 retinopathy for overcoming the failings of mouse models. The calyceal processes of frog photoreceptors, embedded within multiple indentations spanning the entire length of the outer segment (Kennedy and Malicki, 2009), are not as labile as those in primates and they may not be interconnected by the USH1 protein network because they are much further apart than primate calyceal processes. Thus, based on the interspecies differences in the inner–outer segment relationship revealed by this study, a monkey model of USH1 retinopathy would appear to be the most appropriate, particularly for treatment development and testing. This conclusion is timely, as several clinical trials are already being planned for this condition, despite the lack of a relevant model for preclinical validation.

Finally, our results reveal that auditory and visual sensory cells, despite processing different sensory signals—mechanical and photonic inputs, respectively—harbor microvilli or microvillus–cilium structures interconnected by the USH1 protein network. Indeed, the photoreceptor outer segment, considered as a modified cilium, is surrounded by the calyceal processes, like the kinocilium and associated stereocilia of the inner ear hair bundle. The possible mechanosensory role of the USH1-associated network also in the calyceal processes raises the possibility of a connection between the USH1 adhesion network and a putative $Ca^{2+}$-permeable mechanosensitive ion channel in the calyceal processes, similar to that operating in the stereocilia bundle of auditory sensory cells.

## Materials and methods

### Animals

Inner ears and eyes from mice, pigs, monkeys, humans, and frogs were used. RJ Swiss and C57BL6 wild-type mice (Janvier Laboratories) were used. The five USH1 mutant mice (Fig. S1 B) have been described elsewhere (Lefèvre et al., 2008; Caberlotto et al., 2011): (i) *Myo7a*$^{4626SB/4626SB}$ mice, which carry a truncating mutation in the motor head domain (p.Q720X), were provided by K. Steel (Sanger Institute, Cambridge, UK); (ii) *Ush1c*$^{dfcr\text{-}2J/dfcr\text{-}2J}$ mice (The Jackson Laboratory) have one bp deletion causing a frame-shift in a single alternatively transcribed exon (exon C) present in the longer isoform b-harmonin transcripts; (iii) *Cdh23*$^{v2J/v2J}$ mice (The Jackson Laboratory), which display a G>A transition at the first nucleotide position of intron 32 (c.4104 + 1G>A) leading to aberrant splice forms, all predicted to encode proteins that lack the intracellular domain; (iv) *Pcdh15*$^{av3J/av3J}$ mice (The Jackson Laboratory) display a single-base insertion of an adenine residue causing a frame-shift and a premature stop codon after 36 additional amino acid residues (p.E1373RfsX36); and (v) *Ush1*$^{-/-}$ mice carry a deletion of exon 2 causing a frame-shift and a premature stop codon (Caberlotto et al., 2011). For USH2 (Fig. S1 C), the *Usherin* and *Vlgr1* knock-out mice were engineered by deletion of exon 69 (*Ush2a*$^{-/-}$) and exons 2–4 (*Vlgr1*$^{-/-}$; Yagi et al., 2007), respectively. The *Whrn* mutant mice carry a 592-bp deletion causing a frame-shift and a premature stop codon after 58 additional amino acid residues (p.H433fsX58; Mburu et al., 2003).

For RT-qPCR analyses, *C3H rd1/rd1* and *C3H* wild-type mice were provided by T. Leveillard (UMRS 968, Institut de la Vision, Paris, France). Eyes were collected from adult cynomolgus monkeys (*Macaca fascicularis*) housed at the MIRcen platform (CEA/INSERM, Fontenay-aux-Roses, France). These animals were killed as controls in other unrelated experiments. Pig eyes were obtained from the Institut Mutualiste Montsouris (IMM, Paris, France). Adult bullfrogs (*Rana catesbeiana*) and African clawed frogs (*Xenopus laevis*) were obtained from P. Martin (Institut Curie, Paris, France) and the *Xenopus* platform (Université de Rennes, France), respectively. The *Xenopus* embryos, obtained by artificial fertilization, were provided by J.-F. Riou (UPMC Univ. Paris 06, France). Stages were determined according to the normal table for *Xenopus laevis* (Nieuwkoop and Faber, 1967). Human retinas were obtained several hours after death from the Minnesota Lions Eye Bank (Minneapolis, MN). Experiments on animals were performed according to protocols approved by the Animal Use Committees of INSERM, CEA (for monkeys), Institut Pasteur, and the ARVO Statement for the Use of Animals in Ophthalmical and Vision Research.

### RT-qPCR and transcriptome analysis

For RT-PCR analysis, fresh retinas were detached quickly, frozen in liquid nitrogen, and stored at −80°C until processing. Total RNA was prepared from neural retinas and retinal pigment epithelium cells of the various species with the RNeasy kit (QIAGEN). RNA was reverse-transcribed with oligo(dT) primers and the Superscript II enzyme (Invitrogen). RT-qPCR was performed with the SYBR Green master mix real-time core reagents (Applied Biosystems). The relative standard curve method was applied, in which the levels of *USH* and other detected transcripts were normalized with respect to that of the *GAPDH* transcripts measured for the same cDNA sample. Reverse transcription negative controls, containing all RT-PCR reagents except the reverse transcription (−RT), were used (Fig. 1 A). The sequences of the various primers used are listed in Table S1.

Samples for hybridization to Affymetrix GeneChips were prepared and hybridized to MG430.2 arrays, according to the manufacturer's recommendations. Each array was rescaled to have a mean equal to that of a reference array. Robust multichip average (RMA) normalization was performed after background correction, but before summarization. The intensity distribution for each array was reshaped to follow the distribution of the reference array (a synthetic array computed from the median of each feature across arrays). Values are presented as mean ± SEM. ** and *** denote statistically significant differences in Student's *t* test, with $P < 0.01$ and $P < 0.001$, respectively.

### Antibodies and other staining reagents

Rabbit antisera were raised against murine recombinant proteins encompassing different regions of four USH1 and three USH2 proteins (see Fig. 1, A and B): the N-terminal region of harmonin common to all three subclasses of harmonin isoforms (aa 1–71, NCBI Protein database accession no. Q9ES64; antibody H1N), the cytoplasmic region common to all protocadherin-15 isoforms, specifically, CD1, CD2, and CD3 (aa 1403–1460, accession no. Q99PJ1; antibody P1CD1-3), the N-terminal region of sans (aa 1–149, accession no. NP_789817; antibody S1Ank), the cytoplasmic domain of usherin (aa 5064–5193, accession no. Q2QI47; antibody U2CD), the cytoplasmic domain of Vlgr1 (aa 6149–6298, accession no. Q8VHN7; V2CD antibody), and the N-terminal region of the whirlin long isoform (aa 2–506, accession no. Q80VW5-3; antibody W2N; this region has 104 aa in common with the short whirlin isoform; Mburu et al., 2003). Other rabbit antisera were produced against peptide sequences spanning extracellular epitopes of cadherin-23, corresponding to extracellular cadherin (EC) repeat 11 (aa 1161–1174, accession no. NP_075859; antibody C1EC11), and a region in the EC25 repeat (aa 2716–2735, accession no. NP_075859; antibody C1EC25), or the extracellular region next to the transmembrane domain of protocadherin-15 (aa 1330–1345, accession no. Q99PJ1; antibody P1ExJM; see Fig. 1 A). The anti-myosin VIIa antibody M1TN, directed against aa 936–1088 of human myosin VIIa (accession no. NP_000251; El-Amraoui et al., 1996), anti-cadherin-23 antibody C1CDC, directed against aa 3247–3354 of murine cadherin-23 (accession no. NP_075859; Bahloul et al., 2010), and anti-sans antibody S1SAM, directed against aa 369–455 of murine sans (accession no. NP_789817; Caberlotto et al., 2011), have been described elsewhere. The anti-myosin IIIa antibody was directed against the C-terminal region of murine myosin IIIa (aa 1592–1607, accession no. Q8K3H5; M3aC antibody). The anti-espin 1 antibody was directed against a peptide sequence from the murine espin (aa 35–53, accession no. NP_997570; Esp1 antibody). The pan-espin antibody, directed against the C-terminal 378 aa of the rat espin protein (accession no. NP_062568; Zheng et al., 2000), was provided by J. Bartles (Northwestern University Feinberg School of Medicine, Chicago, IL).

These antibodies were affinity purified with the corresponding antigens coupled to an NHS-column (GE Healthcare). The specificity of each anti-USH1 or anti-USH2 antibody was checked by immunofluorescence labeling on cochleas from the corresponding Ush1 or Ush2 mutant mouse (Fig. S1, A–C).

The following primary antibodies and reagents were used: mouse monoclonal anti-glutamylated tubulin (GT335; ALX-804-885; Enzo Life Sciences), mouse anti-rhodopsin (MAB5316; EMD Millipore), goat polyclonal anti-cone opsin (sc-22117; Santa Cruz Biotechnology, Inc.), and rabbit polyclonal anti-PMCA2 (SWANT, Switzerland; and sc-22073, Santa Cruz Biotechnology, Inc.) antibodies. TRITC-phalloidin (Sigma-Aldrich) and DAPI (1 µg/ml; Sigma-Aldrich) were used to label F-actin and cell nuclei, respectively.

**Immunofluorescence experiments**

Samples (whole-mount preparations of the organ of Corti, flat-mount retinas, or retina cryosections) were processed for immunofluorescence as described previously (Legendre et al., 2008). Inner ears and/or eyes, obtained from non-perfused or perfused animals, were dissected and fixed by incubation in 4% paraformaldehyde (PFA) in phosphate-buffered saline (PBS) for 1–3 h at 4°C. For cryosectioning, samples were immersed in graded sucrose solutions (15–30% wt/vol) and embedded in tissue-freezing medium, and 10-µm-thick sections were cut. For retinal flat mounts, the retinas were carefully excised from the eye wall and small pieces (3 mm × 3 mm) were processed for immunofluorescence. In brief, samples were blocked in 10% bovine serum albumin (BSA) in PBS, incubated overnight with the appropriate primary antibody at 4°C, rinsed in PBS, incubated with the appropriate secondary antibody for 1 h at room temperature, rinsed in PBS, and counterstained with DAPI. Secondary antibodies were as follows: Alexa Fluor 488 goat anti–rabbit IgG; Alexa Fluor 488 goat anti–mouse IgG; Alexa Fluor 594 goat anti–rabbit IgG; Alexa Fluor 594 goat anti–mouse IgG; Alexa Fluor 647 donkey anti–mouse IgG, all from Invitrogen; DyLight 649-donkey anti–mouse IgG and Cy3 donkey anti-mouse IgG were from Jackson ImmunoResearch Laboratories, Inc.

For double-labeling experiments with two rabbit primary antibodies, the fixed tissue samples were sequentially incubated with the first primary antibody (anti-USH2) for 2 h, and then with an anti–rabbit Alexa Fluor 594–conjugated secondary antibody (Invitrogen) for 1 h at room temperature. Sections were then fixed by incubation for 15 min in 4% PFA at room temperature, and incubated with the second primary antibody (anti-USH1) in the presence of the mouse monoclonal anti-glutamylated tubulin antibody overnight at 4°C, and then with anti–rabbit Alexa Fluor 488– and anti–mouse DyLight 649–conjugated secondary antibodies (Invitrogen) for 1 h at room temperature, to visualize the USH1 protein and the connecting cilium, respectively. The second primary antibody was omitted as a negative control. Stained cells were mounted with FluorSave reagent (EMD Millipore) for imaging using a confocal laser-scanning microscope (model LSM 700, 63× oil-immersion lens, 1.40 NA, LSM 700 software; Carl Zeiss) or a FluoView microscope (model FV1000, 60× oil-immersion lens, 1.42 NA, NIS-Elements software; Olympus) at room temperature. Tiff images were obtained using ImageJ (v1.43; National Institutes of Health, Bethesda, MD) or LSM 700 software. z-sections were projected on a single plane using maximum intensity under z-project function, and finally converted to an RGB color mode. Brightness and contrast adjustments to images, and final composite images were subsequently made using or Photoshop CS3 (v10.0; Adobe).

**Scanning electron microscopy**

The neuroretinas obtained from perfused mice, macaques, and (non-perfused) adult *Xenopus* were postfixed by immersion in 2.5% glutaraldehyde in 0.1 M cacodylate buffer (pH 7.3) for 2 h at room temperature. For *Xenopus* tadpoles, embryos at various developmental stages were fixed by incubation in 4% PFA/0.1 M phosphate buffer/1 mM $CaCl_2$ for 1 h at room temperature, then postfixed by incubation in 2.5% glutaraldehyde in 0.1 M cacodylate buffer for 2 h. The tadpoles were washed in PBS and embedded in 4% agar (Sigma-Aldrich), and 250–350-µm-thick sections of the heads were cut perpendicular to the long axis of the tadpole.

Adult neuroretinas and vibratome sections of *Xenopus* tadpoles were then prepared for scanning electron microscopy, according to the OTOTO protocol, as described previously (Furness et al., 2008). The samples were dehydrated in ethanol, dried to critical point, and fractured along a plane passing through the long axis of the photoreceptors. The fragments were mounted on aluminum stubs with double-adhesive carbon tape, and examined under a scanning microscope (JSM 6700F; JEOL Ltd.). We performed a morphometric analysis on scanning electron micrographs showing well-preserved macaque cone and rod photoreceptors to determine several features of the calyceal processes (see Fig. 4 F).

**Pre-embedding immunoelectron microscopy**

Immunolabeling was performed with a pre-embedding immunoelectron microscopy technique, modified from a previously described technique (Hirano et al., 2011). In brief, eyecups were infiltrated with 10% sucrose for 1 h at 4°C; retinas were removed, immersed in graded sucrose solutions, and frozen and thawed three times to improve antibody penetration. We cut 50-µm-thick vibratome sections in cold PBS, pH 7.4. After aldehyde neutralization in 50 mM glycine/PBS, sections were immersed in 10% goat serum/1% BSA/PBS, incubated for 4 d with the anti–cadherin-23 or anti–protocadherin-15 antibody in PBS supplemented with 0.5% BSA and 0.1% acetylated BSA (BSA-c; Aurion), then overnight with the goat anti–rabbit antibody conjugated to 0.8-nm gold particles (Aurion) in the same buffer; sections were postfixed in 2% glutaraldehyde followed by 0.2% $OsO_4$. They were then subjected to silver enhancement (Aurion), dehydrated and embedded in Epon/Araldite. Alternatively, retinas were neutralized in 50 mM glycine/PBS, permeabilized by incubation for 10 min in cold 0.05% Tween 20/PBS, blocked, and incubated with antibodies, postfixed, subjected to silver enhancement, dehydrated and embedded in plastic, as described above. Ultrathin sections were cut with an Ultramicrotome (Leica) and contrast-stained with modified Sato's lead. Images were acquired with 912 Omega (Carl Zeiss) and CM100 (Philips) transmission electron microscopes, and analyzed with ImageJ.

For the quantification of immunogold labeling, we used only micrographs with photoreceptor profiles displaying clearly distinguishable inner and outer segments and calyceal processes. We focused on four subcellular compartments: the inner segment, the outer segment, the calyceal processes–outer segment interface, and the inner–outer segment interface (see Fig. 4, A–D). Most (≥90%) of the gold particles specific to cadherin-23 and protocadherin-15 were found close to the plasma membrane in each of the compartments analyzed, as expected for membrane-associated epitopes. We compared the distribution of gold particles between compartments by expressing labeling intensity as the relative labeling index (RLI), as described previously (Mayhew et al., 2009). RLI provides a measurement of the degree to which each photoreceptor compartment is labeled with respect to what would be expected for random labeling, and values of RLI > 1 for a compartment indicate specific enrichment in that compartment. RLI was calculated as $N_{obs}/N_{exp}$, where $N_{obs}$ denotes the number of particles counted for the compartment concerned and $N_{exp}$ is the expected number of particles assuming a random distribution of labeling, or: $RLI_c = N_{obs(c)}/(N_{tot} \times L_c/L_{tot})$, where $L_{tot}$ and $N_{tot}$ denote the total length measured and the total number of particles counted, $L_{(c)}$ and $N_{obs(c)}$ the length of compartment *C* and the particles associated with it, respectively. The silver-enhanced nanogold particles were assigned to each of these membrane compartments, and the length (L) of each compartment was measured in ImageJ to obtain particle densities (N/L, expressed as particles/µm). We counted a total of 285 immunogold-labeled particles for cadherin-23 and 533 for protocadherin-15, with $\chi^2$ values as follows: 72 for cadherin-23 (cones), 145 for cadherin-23 (rods), 381 for protocadherin-15 (cones), and 681 for protocadherin-15 (rods). The relative contribution of each compartment to the photoreceptor profile length varied between micrographs and, in the same micrograph, between photoreceptors, as a function of cutting angle orientation. *** denotes statistically significant enrichment in $\chi^2$ test ($P < 0.001$), as previously reported (Mayhew et al., 2009).

**Co-immunoprecipitation experiments**

For each immunoprecipitation (IP) experiment, ∼30 *Xenopus* retinas were collected in binding buffer (50 mM Tris, pH 7.5, 200 mM KCl, 1 mM EGTA, 1 mM MgATP, 0.05% DDM, 3% glycerol, and 0.01% SDS) supplemented with protease inhibitor cocktail (Roche), and the samples were then cleared by ultracentrifugation. Equal amounts of the solubilized protein extracts were incubated with the anti-S1SAM antibody, the anti-S1Ank antibody, or with the binding buffer solution alone. After 3 h of incubation at 4°C, 30 µl of a pre-equilibrated protein G solution (Thermo Fisher Scientific) was added to each sample, and samples were incubated for an additional 3 h at 4°C. After three washes in binding buffer, bound proteins were eluted in binding buffer supplemented with 200 mM KCl and 1% Triton X-100. Equivalent amounts of immunoprecipitate were run on 4–12% NuPAGE gels (Invitrogen) and subjected to Western blot analysis. Horseradish peroxidase (HRP)–conjugated goat anti–rabbit or anti–mouse antibodies (Jackson ImmunoResearch Laboratories, Inc.) and the ECL chemiluminescence system (Thermo Fisher Scientific) were used for detection.

### Disruption of calyceal process–outer segment links by treatment with subtilisin and BAPTA

Adult *Xenopus* eyes were dissected in Ringer solution (110 mM NaCl, 2.5 mM KCl, 10 mM glucose, 1.6 mM $MgCl_2$, 1 mM $CaCl_2$, and 10 mM Hepes, pH 7.4). The neural retina was separated from the retinal pigment epithelium and incubated at room temperature in (i) Ringer solution alone for 20 min, (ii) Ringer solution containing 50 µg/ml subtilisin (Protease XXIV; Sigma-Aldrich) for 20 min, or (iii) Ringer solution containing 50 µg/ml subtilisin for 10 min, followed by $Ca^{2+}$-free Ringer solution containing 5 mM BAPTA for 10 min. The retinas were then fixed and processed for scanning electron microscopy, as described above.

### Online supplemental material

Fig. S1 shows the specificity of anti-USH1 and anti-USH2 antibodies. Fig. S2 illustrates the presence of the calyceal processes and their F-actin–labeled roots in the inner segments, which are well developed in macaque and pig, but absent from mouse and rat photoreceptors. Fig. S3 illustrates the intense USH1 proteins labeling at the inner–outer segment junction in rod photoreceptors, and the preservation of the calyceal processes in macaque photoreceptors when the neural retina is obtained from an animal perfused with the fixative solution. Fig. S4 illustrates the disruption of the calyceal processes in human and pig photoreceptors, and their preservation in frog photoreceptors, in the absence of perfusion with the fixative solution. Table S1 lists the primers used to detect USH1 and USH2 gene transcripts. Online supplemental material is available at http://www.jcb.org/cgi/content/full/jcb.201202012/DC1.

We thank J. Boutet de Monvel for his critical comments on the manuscript, T. Léveillard for his help with the transcriptomic analysis of USH1 and USH2 genes in the retina, the MIRcen platform (CEA/INSERM) for monkey eyes, and J.-F. Riou and P. Martin for providing us with the *Xenopus* tadpoles and adult bullfrogs, respectively.

This research was funded by the European Union Seventh Framework Program, under grant agreement HEALTH-F2-2010-242013 (TREATRUSH), LHW-Stiftung, Fondation Raymonde & Guy Strittmatter, ERC, Fighting Blindness, FAUN Stiftung (Suchert Foundation), Conny Maeva Charitable Foundation, Fondation Orange, ERC grant 294570-hair bundle, and Louis-Jeantet Foundation (C. Petit), the French State program "Investissements d'Avenir" managed by the Agence Nationale de la Recherche (grant reference: ANR-10-LABX-65), "the Foundation Fighting Blindness Paris Center Grant" and the Fondation Voir et Entendre (C. Petit and J.-A. Sahel), and an ANR-07-MRARE-009-01 grant to A. El-Amraoui.

Submitted: 2 February 2012
Accepted: 7 September 2012

## References

Adato, A., V. Michel, Y. Kikkawa, J. Reiners, K.N. Alagramam, D. Weil, H. Yonekawa, U. Wolfrum, A. El-Amraoui, and C. Petit. 2005. Interactions in the network of Usher syndrome type 1 proteins. *Hum. Mol. Genet.* 14:347–356. http://dx.doi.org/10.1093/hmg/ddi031

Ahmed, Z.M., S. Riazuddin, J. Ahmad, S.L. Bernstein, Y. Guo, M.F. Sabar, P. Sieving, S. Riazuddin, A.J. Griffith, T.B. Friedman, et al. 2003. *PCDH15* is expressed in the neurosensory epithelium of the eye and ear and mutant alleles are responsible for both USH1F and DFNB23. *Hum. Mol. Genet.* 12:3215–3223. http://dx.doi.org/10.1093/hmg/ddg358

Ahmed, Z.M., S. Kjellstrom, R.J. Haywood-Watson, R.A. Bush, L.L. Hampton, J.F. Battey, S. Riazuddin, G. Frolenkov, P.A. Sieving, and T.B. Friedman. 2008. Double homozygous waltzer and Ames waltzer mice provide no evidence of retinal degeneration. *Mol. Vis.* 14:2227–2236.

Bahloul, A., V. Michel, J.P. Hardelin, S. Nouaille, S. Hoos, A. Houdusse, P. England, and C. Petit. 2010. Cadherin-23, myosin VIIa and harmonin, encoded by Usher syndrome type I genes, form a ternary complex and interact with membrane phospholipids. *Hum. Mol. Genet.* 19:3557–3565. http://dx.doi.org/10.1093/hmg/ddq271

Ball, S.L., D. Bardenstein, and K.N. Alagramam. 2003. Assessment of retinal structure and function in Ames waltzer mice. *Invest. Ophthalmol. Vis. Sci.* 44:3986–3992. http://dx.doi.org/10.1167/iovs.02-1009

Boëda, B., A. El-Amraoui, A. Bahloul, R. Goodyear, L. Daviet, S. Blanchard, I. Perfettini, K.R. Fath, S. Shorte, J. Reiners, et al. 2002. Myosin VIIa, harmonin and cadherin 23, three Usher I gene products that cooperate to shape the sensory hair cell bundle. *EMBO J.* 21:6689–6699. http://dx.doi.org/10.1093/emboj/cdf689

Bonnet, C., and A. El-Amraoui. 2012. Usher syndrome (sensorineural deafness and retinitis pigmentosa): pathogenesis, molecular diagnosis and therapeutic approaches. *Curr. Opin. Neurol.* 25:42–49. http://dx.doi.org/10.1097/WCO.0b013e32834ef8b2

Bowes, C., T. Li, M. Danciger, L.C. Baxter, M.L. Applebury, and D.B. Farber. 1990. Retinal degeneration in the rd mouse is caused by a defect in the beta subunit of rod cGMP-phosphodiesterase. *Nature*. 347:677–680. http://dx.doi.org/10.1038/347677a0

Brown, P.K., I.R. Gibbons, and G. Wald. 1963. The visual cells and visual pigment of the mudpuppy, *Necturus*. *J. Cell Biol.* 19:79–106. http://dx.doi.org/10.1083/jcb.19.1.79

Caberlotto, E., V. Michel, I. Foucher, A. Bahloul, R.J. Goodyear, E. Pepermans, N. Michalski, I. Perfettini, O. Alegria-Prévot, S. Chardenoux, et al. 2011. Usher type 1G protein sans is a critical component of the tip-link complex, a structure controlling actin polymerization in stereocilia. *Proc. Natl. Acad. Sci. USA*. 108:5825–5830. http://dx.doi.org/10.1073/pnas.1017114108

Caride, A.J., A.R. Penheiter, A.G. Filoteo, Z. Bajzer, A. Enyedi, and J.T. Penniston. 2001. The plasma membrane calcium pump displays memory of past calcium spikes. Differences between isoforms 2b and 4b. *J. Biol. Chem.* 276:39797–39804. http://dx.doi.org/10.1074/jbc.M104380200

Cohen, A.I. 1963. Vertebrate retinal cells and their organization. *Biol. Rev. Camb. Philos. Soc.* 38:427–459. http://dx.doi.org/10.1111/j.1469-185X.1963.tb00789.x

Ebermann, I., H.P. Scholl, P. Charbel Issa, E. Becirovic, J. Lamprecht, B. Jurklies, J.M. Millán, E. Aller, D. Mitter, and H. Bolz. 2007. A novel gene for Usher syndrome type 2: mutations in the long isoform of whirlin are associated with retinitis pigmentosa and sensorineural hearing loss. *Hum. Genet.* 121:203–211. http://dx.doi.org/10.1007/s00439-006-0304-0

Eckmiller, M.S. 1987. Cone outer segment morphogenesis: taper change and distal invaginations. *J. Cell Biol.* 105:2267–2277. http://dx.doi.org/10.1083/jcb.105.5.2267

El-Amraoui, A., and C. Petit. 2005. Usher I syndrome: unravelling the mechanisms that underlie the cohesion of the growing hair bundle in inner ear sensory cells. *J. Cell Sci.* 118:4593–4603. http://dx.doi.org/10.1242/jcs.02636

El-Amraoui, A., and C. Petit. 2010. Cadherins as targets for genetic diseases. *Cold Spring Harb. Perspect. Biol.* 2:a003095. http://dx.doi.org/10.1101/cshperspect.a003095

El-Amraoui, A., I. Sahly, S. Picaud, J. Sahel, M. Abitbol, and C. Petit. 1996. Human Usher 1B/mouse shaker-1: the retinal phenotype discrepancy explained by the presence/absence of myosin VIIA in the photoreceptor cells. *Hum. Mol. Genet.* 5:1171–1178. http://dx.doi.org/10.1093/hmg/5.8.1171

El-Amraoui, A., J.-S. Schonn, P. Küssel-Andermann, S. Blanchard, C. Desnos, J.-P. Henry, U. Wolfrum, F. Darchen, and C. Petit. 2002. MyRIP, a novel Rab effector, enables myosin VIIa recruitment to retinal melanosomes. *EMBO Rep.* 3:463–470. http://dx.doi.org/10.1093/embo-reports/kvf090

Elledge, H.M., P. Kazmierczak, P. Clark, J.S. Joseph, A. Kolatkar, P. Kuhn, and U. Müller. 2010. Structure of the N terminus of cadherin 23 reveals a new adhesion mechanism for a subset of cadherin superfamily members. *Proc. Natl. Acad. Sci. USA*. 107:10708–10712. http://dx.doi.org/10.1073/pnas.1006284107

Eudy, J.D., M.D. Weston, S. Yao, D.M. Hoover, H.L. Rehm, M. Ma-Edmonds, D. Yan, I. Ahmad, J.J. Cheng, C. Ayuso, et al. 1998. Mutation of a gene encoding a protein with extracellular matrix motifs in Usher syndrome type IIa. *Science*. 280:1753–1757. http://dx.doi.org/10.1126/science.280.5370.1753

Flores-Guevara, R., F. Renault, N. Loundon, S. Marlin, B. Pelosse, M. Momtchilova, M. Auzoux-Chevé, A.I. Vermersch, and P. Richard. 2009. Usher syndrome type 1: early detection of electroretinographic changes. *Eur. J. Paediatr. Neurol.* 13:505–507. http://dx.doi.org/10.1016/j.ejpn.2008.10.002

Furness, D.N., Y. Katori, B. Nirmal Kumar, and C.M. Hackney. 2008. The dimensions and structural attachments of tip links in mammalian cochlear hair cells and the effects of exposure to different levels of extracellular calcium. *Neuroscience*. 154:10–21. http://dx.doi.org/10.1016/j.neuroscience.2008.02.010

Giacomello, M., A. De Mario, R. Lopreiato, S. Primerano, M. Campeol, M. Brini, and E. Carafoli. 2011. Mutations in PMCA2 and hereditary deafness: a molecular analysis of the pump defect. *Cell Calcium*. 50:569–576. http://dx.doi.org/10.1016/j.ceca.2011.09.004

Gibbs, D., S.M. Azarian, C. Lillo, J. Kitamoto, A.E. Klomp, K.P. Steel, R.T. Libby, and D.S. Williams. 2004. Role of myosin VIIa and Rab27a in the motility and localization of RPE melanosomes. *J. Cell Sci.* 117:6473–6483. http://dx.doi.org/10.1242/jcs.01580

Goodyear, R.J., and G.P. Richardson. 2003. A novel antigen sensitive to calcium chelation that is associated with the tip links and kinocilial links of sensory hair bundles. *J. Neurosci.* 23:4878–4887.

Grati, M., and B. Kachar. 2011. Myosin VIIa and sans localization at stereocilia upper tip-link density implicates these Usher syndrome proteins in

mechanotransduction. *Proc. Natl. Acad. Sci. USA*. 108:11476–11481. http://dx.doi.org/10.1073/pnas.1104161108

Grillet, N., W. Xiong, A. Reynolds, P. Kazmierczak, T. Sato, C. Lillo, R.A. Dumont, E. Hintermann, A. Sczaniecka, M. Schwander, et al. 2009. Harmonin mutations cause mechanotransduction defects in cochlear hair cells. *Neuron*. 62:375–387. http://dx.doi.org/10.1016/j.neuron.2009.04.006

Hasson, T., M.B. Heintzelman, J. Santos-Sacchi, D.P. Corey, and M.S. Mooseker. 1995. Expression in cochlea and retina of myosin VIIa, the gene product defective in Usher syndrome type 1B. *Proc. Natl. Acad. Sci. USA*. 92:9815–9819. http://dx.doi.org/10.1073/pnas.92.21.9815

Haywood-Watson, R.J. II, Z.M. Ahmed, S. Kjellstrom, R.A. Bush, Y. Takada, L.L. Hampton, J.F. Battey, P.A. Sieving, and T.B. Friedman. 2006. Ames Waltzer deaf mice have reduced electroretinogram amplitudes and complex alternative splicing of Pcdh15 transcripts. *Invest. Ophthalmol. Vis. Sci.* 47:3074–3084. http://dx.doi.org/10.1167/iovs.06-0108

Heissler, S.M., and D.J. Manstein. 2012. Functional characterization of the human myosin-7a motor domain. *Cell. Mol. Life Sci.* 69:299–311. http://dx.doi.org/10.1007/s00018-011-0749-8

Henn, A., and E.M. De La Cruz. 2005. Vertebrate myosin VIIb is a high duty ratio motor adapted for generating and maintaining tension. *J. Biol. Chem.* 280:39665–39676. http://dx.doi.org/10.1074/jbc.M507667200

Hirano, A.A., J.H. Brandstätter, C.W. Morgans, and N.C. Brecha. 2011. SNAP25 expression in mammalian retinal horizontal cells. *J. Comp. Neurol.* 519:972–988. http://dx.doi.org/10.1002/cne.22562

Höfer, D., and D. Drenckhahn. 1993. Molecular heterogeneity of the actin filament cytoskeleton associated with microvilli of photoreceptors, Müller's glial cells and pigment epithelial cells of the retina. *Histochemistry*. 99:29–35. http://dx.doi.org/10.1007/BF00268017

Inoue, A., and M. Ikebe. 2003. Characterization of the motor activity of mammalian myosin VIIA. *J. Biol. Chem.* 278:5478–5487. http://dx.doi.org/10.1074/jbc.M210489200

Jacobson, S.G., A.V. Cideciyan, D. Gibbs, A. Sumaroka, A.J. Roman, T.S. Aleman, S.B. Schwartz, M.B. Olivares, R.C. Russell, J.D. Steinberg, et al. 2011. Retinal disease course in Usher syndrome 1B due to MYO7A mutations. *Invest. Ophthalmol. Vis. Sci.* 52:7924–7936. http://dx.doi.org/10.1167/iovs.11-8313

Johnson, K.R., L.H. Gagnon, L.S. Webb, L.L. Peters, N.L. Hawes, B. Chang, and Q.Y. Zheng. 2003. Mouse models of USH1C and DFNB18: phenotypic and molecular analyses of two new spontaneous mutations of the Ush1c gene. *Hum. Mol. Genet.* 12:3075–3086. http://dx.doi.org/10.1093/hmg/ddg332

Kazmierczak, P., H. Sakaguchi, J. Tokita, E.M. Wilson-Kubalek, R.A. Milligan, U. Müller, and B. Kachar. 2007. Cadherin 23 and protocadherin 15 interact to form tip-link filaments in sensory hair cells. *Nature*. 449:87–91. http://dx.doi.org/10.1038/nature06091

Kennedy, B., and J. Malicki. 2009. What drives cell morphogenesis: a look inside the vertebrate photoreceptor. *Dev. Dyn.* 238:2115–2138. http://dx.doi.org/10.1002/dvdy.22010

Lagziel, A., Z.M. Ahmed, J.M. Schultz, R.J. Morell, I.A. Belyantseva, and T.B. Friedman. 2005. Spatiotemporal pattern and isoforms of cadherin 23 in wild type and waltzer mice during inner ear hair cell development. *Dev. Biol.* 280:295–306. http://dx.doi.org/10.1016/j.ydbio.2005.01.015

Lagziel, A., N. Overlack, S.L. Bernstein, R.J. Morell, U. Wolfrum, and T.B. Friedman. 2009. Expression of cadherin 23 isoforms is not conserved: implications for a mouse model of Usher syndrome type 1D. *Mol. Vis.* 15:1843–1857.

Lefèvre, G., V. Michel, D. Weil, L. Lepelletier, E. Bizard, U. Wolfrum, J.P. Hardelin, and C. Petit. 2008. A core cochlear phenotype in USH1 mouse mutants implicates fibrous links of the hair bundle in its cohesion, orientation and differential growth. *Development*. 135:1427–1437. http://dx.doi.org/10.1242/dev.012922

Legendre, K., S. Safieddine, P. Küssel-Andermann, C. Petit, and A. El-Amraoui. 2008. alphaII-betaV spectrin bridges the plasma membrane and cortical lattice in the lateral wall of the auditory outer hair cells. *J. Cell Sci.* 121:3347–3356. http://dx.doi.org/10.1242/jcs.028134

Lentz, J.J., W.C. Gordon, H.E. Farris, G.H. MacDonald, D.E. Cunningham, C.A. Robbins, B.L. Tempel, N.G. Bazan, E.W. Rubel, E.C. Oesterle, and B.J. Keats. 2010. Deafness and retinal degeneration in a novel USH1C knock-in mouse model. *Dev. Neurobiol.* 70:253–267. http://dx.doi.org/10.1002/dneu.20771

Libby, R.T., and K.P. Steel. 2001. Electroretinographic anomalies in mice with mutations in Myo7a, the gene involved in human Usher syndrome type 1B. *Invest. Ophthalmol. Vis. Sci.* 42:770–778.

Libby, R.T., J. Kitamoto, R.H. Holme, D.S. Williams, and K.P. Steel. 2003. Cdh23 mutations in the mouse are associated with retinal dysfunction but not retinal degeneration. *Exp. Eye Res.* 77:731–739. http://dx.doi.org/10.1016/j.exer.2003.07.007

Lin-Jones, J., and B. Burnside. 2007. Retina-specific protein fascin 2 is an actin cross-linker associated with actin bundles in photoreceptor inner segments and calycal processes. *Invest. Ophthalmol. Vis. Sci.* 48:1380–1388. http://dx.doi.org/10.1167/iovs.06-0763

Lin-Jones, J., E. Parker, M. Wu, A. Dosé, and B. Burnside. 2004. Myosin 3A transgene expression produces abnormal actin filament bundles in transgenic *Xenopus laevis* rod photoreceptors. *J. Cell Sci.* 117:5825–5834. http://dx.doi.org/10.1242/jcs.01512

Liu, X., G. Vansant, I.P. Udovichenko, U. Wolfrum, and D.S. Williams. 1997. Myosin VIIa, the product of the Usher 1B syndrome gene, is concentrated in the connecting cilia of photoreceptor cells. *Cell Motil. Cytoskeleton*. 37:240–252. http://dx.doi.org/10.1002/(SICI)1097-0169(1997)37:3<240::AID-CM6>3.0.CO;2-A

Liu, X., B. Ondek, and D.S. Williams. 1998. Mutant myosin VIIa causes defective melanosome distribution in the RPE of shaker-1 mice. *Nat. Genet.* 19:117–118. http://dx.doi.org/10.1038/470

Liu, X., I.P. Udovichenko, S.D. Brown, K.P. Steel, and D.S. Williams. 1999. Myosin VIIa participates in opsin transport through the photoreceptor cilium. *J. Neurosci.* 19:6267–6274.

Maerker, T., E. van Wijk, N. Overlack, F.F. Kersten, J. McGee, T. Goldmann, E. Sehn, R. Roepman, E.J. Walsh, H. Kremer, and U. Wolfrum. 2008. A novel Usher protein network at the periciliary reloading point between molecular transport machineries in vertebrate photoreceptor cells. *Hum. Mol. Genet.* 17:71–86. http://dx.doi.org/10.1093/hmg/ddm285

Malm, E., V. Ponjavic, C. Möller, W.J. Kimberling, and S. Andréasson. 2011a. Phenotypes in defined genotypes including siblings with Usher syndrome. *Ophthalmic Genet.* 32:65–74. http://dx.doi.org/10.3109/13816810.2010.536064

Malm, E., V. Ponjavic, C. Möller, W.J. Kimberling, E.S. Stone, and S. Andréasson. 2011b. Alteration of rod and cone function in children with Usher syndrome. *Eur. J. Ophthalmol.* 21:30–38. http://dx.doi.org/10.5301/EJO.2010.5433

Mayhew, T.M., C. Mühlfeld, D. Vanhecke, and M. Ochs. 2009. A review of recent methods for efficiently quantifying immunogold and other nanoparticles using TEM sections through cells, tissues and organs. *Ann. Anat.* 191:153–170. http://dx.doi.org/10.1016/j.aanat.2008.11.001

Mburu, P., M. Mustapha, A. Varela, D. Weil, A. El-Amraoui, R.H. Holme, A. Rump, R.E. Hardisty, S. Blanchard, R.S. Coimbra, et al. 2003. Defects in whirlin, a PDZ domain molecule involved in stereocilia elongation, cause deafness in the whirler mouse and families with DFNB31. *Nat. Genet.* 34:421–428. http://dx.doi.org/10.1038/ng1208

Michalski, N., V. Michel, E. Caberlotto, G.M. Lefèvre, A.F.J. van Aken, J.-Y. Tinevez, E. Bizard, C. Houbron, D. Weil, J.-P. Hardelin, et al. 2009. Harmonin-b, an actin-binding scaffold protein, is involved in the adaptation of mechanoelectrical transduction by sensory hair cells. *Pflugers Arch.* 459:115–130. http://dx.doi.org/10.1007/s00424-009-0711-x

Michel, V., R.J. Goodyear, D. Weil, W. Marcotti, I. Perfettini, U. Wolfrum, C.J. Kros, G.P. Richardson, and C. Petit. 2005. Cadherin 23 is a component of the transient lateral links in the developing hair bundles of cochlear sensory cells. *Dev. Biol.* 280:281–294. http://dx.doi.org/10.1016/j.ydbio.2005.01.014

Nieuwkoop, P.D., and J. Faber. 1967. Normal table of *Xenopus laevis*. North Holland Publishing Co., Amsterdam, The Netherlands.

O'Connor, P., and B. Burnside. 1981. Actin-dependent cell elongation in teleost retinal rods: requirement for actin filament assembly. *J. Cell Biol.* 89:517–524. http://dx.doi.org/10.1083/jcb.89.3.517

Pagh-Roehl, K., E. Wang, and B. Burnside. 1992. Shortening of the calycal process actin cytoskeleton is correlated with myoid elongation in teleost rods. *Exp. Eye Res.* 55:735–746. http://dx.doi.org/10.1016/0014-4835(92)90178-U

Pan, L., and M. Zhang. 2012. Structures of usher syndrome 1 proteins and their complexes. *Physiology (Bethesda)*. 27:25–42. http://dx.doi.org/10.1152/physiol.00037.2011

Pan, L., J. Yan, L. Wu, and M. Zhang. 2009. Assembling stable hair cell tip link complex via multidentate interactions between harmonin and cadherin 23. *Proc. Natl. Acad. Sci. USA*. 106:5575–5580. http://dx.doi.org/10.1073/pnas.0901819106

Petit, C. 2001. Usher syndrome: from genetics to pathogenesis. *Annu. Rev. Genomics Hum. Genet.* 2:271–297. http://dx.doi.org/10.1146/annurev.genom.2.1.271

Petit, C., and G.P. Richardson. 2009. Linking genes underlying deafness to hair-bundle development and function. *Nat. Neurosci.* 12:703–710. http://dx.doi.org/10.1038/nn.2330

Reiners, J., and U. Wolfrum. 2006. Molecular analysis of the supramolecular usher protein complex in the retina. Harmonin as the key protein of the Usher syndrome. *Adv. Exp. Med. Biol.* 572:349–353. http://dx.doi.org/10.1007/0-387-32442-9_49

Reiners, J., B. Reidel, A. El-Amraoui, B. Boëda, I. Huber, C. Petit, and U. Wolfrum. 2003. Differential distribution of harmonin isoforms and their possible role in Usher-1 protein complexes in mammalian photoreceptor cells. *Invest. Ophthalmol. Vis. Sci.* 44:5006–5015. http://dx.doi.org/10.1167/iovs.03-0483

Reiners, J., T. Märker, K. Jürgens, B. Reidel, and U. Wolfrum. 2005. Photoreceptor expression of the Usher syndrome type 1 protein protocadherin 15 (USH1F) and its interaction with the scaffold protein harmonin (USH1C). *Mol. Vis.* 11:347–355.

Richardson, G.P., J.B. de Monvel, and C. Petit. 2011. How the genetics of deafness illuminates auditory physiology. *Annu. Rev. Physiol.* 73:311–334. http://dx.doi.org/10.1146/annurev-physiol-012110-142228

Siemens, J., P. Kazmierczak, A. Reynolds, M. Sticker, A. Littlewood-Evans, and U. Müller. 2002. The Usher syndrome proteins cadherin 23 and harmonin form a complex by means of PDZ-domain interactions. *Proc. Natl. Acad. Sci. USA*. 99:14946–14951. http://dx.doi.org/10.1073/pnas.232579599

Sotomayor, M., W.A. Weihofen, R. Gaudet, and D.P. Corey. 2010. Structural determinants of cadherin-23 function in hearing and deafness. *Neuron*. 66:85–100. http://dx.doi.org/10.1016/j.neuron.2010.03.028

Steinberg, R.H., S.K. Fisher, and D.H. Anderson. 1980. Disc morphogenesis in vertebrate photoreceptors. *J. Comp. Neurol.* 190:501–508. http://dx.doi.org/10.1002/cne.901900307

Sung, C.H., and J.Z. Chuang. 2010. The cell biology of vision. *J. Cell Biol.* 190:953–963. http://dx.doi.org/10.1083/jcb.201006020

Weil, D., A. El-Amraoui, S. Masmoudi, M. Mustapha, Y. Kikkawa, S. Lainé, S. Delmaghani, A. Adato, S. Nadifi, Z.B. Zina, et al. 2003. Usher syndrome type I G (USH1G) is caused by mutations in the gene encoding SANS, a protein that associates with the USH1C protein, harmonin. *Hum. Mol. Genet.* 12:463–471. http://dx.doi.org/10.1093/hmg/ddg051

Weston, M.D., M.W. Luijendijk, K.D. Humphrey, C. Möller, and W.J. Kimberling. 2004. Mutations in the VLGR1 gene implicate G-protein signaling in the pathogenesis of Usher syndrome type II. *Am. J. Hum. Genet.* 74:357–366. http://dx.doi.org/10.1086/381685

Williams, D.S., K.A. Linberg, D.K. Vaughan, R.N. Fariss, and S.K. Fisher. 1988. Disruption of microfilament organization and deregulation of disk membrane morphogenesis by cytochalasin D in rod and cone photoreceptors. *J. Comp. Neurol.* 272:161–176. http://dx.doi.org/10.1002/cne.902720202

Williams, D.S., T.S. Aleman, C. Lillo, V.S. Lopes, L.C. Hughes, E.M. Stone, and S.G. Jacobson. 2009. Harmonin in the murine retina and the retinal phenotypes of Ush1c-mutant mice and human USH1C. *Invest. Ophthalmol. Vis. Sci.* 50:3881–3889. http://dx.doi.org/10.1167/iovs.08-3358

Wu, L., L. Pan, Z. Wei, and M. Zhang. 2011. Structure of MyTH4-FERM domains in myosin VIIa tail bound to cargo. *Science*. 331:757–760. http://dx.doi.org/10.1126/science.1198848

Yagi, H., H. Tokano, M. Maeda, T. Takabayashi, T. Nagano, H. Kiyama, S. Fujieda, K. Kitamura, and M. Sato. 2007. Vlgr1 is required for proper stereocilia maturation of cochlear hair cells. *Genes Cells*. 12:235–250. http://dx.doi.org/10.1111/j.1365-2443.2007.01046.x

Yan, J., L. Pan, X. Chen, L. Wu, and M. Zhang. 2010. The structure of the harmonin/sans complex reveals an unexpected interaction mode of the two Usher syndrome proteins. *Proc. Natl. Acad. Sci. USA*. 107:4040–4045. http://dx.doi.org/10.1073/pnas.0911385107

Zheng, L., G. Sekerková, K. Vranich, L.G. Tilney, E. Mugnaini, and J.R. Bartles. 2000. The deaf jerker mouse has a mutation in the gene encoding the espin actin-bundling proteins of hair cell stereocilia and lacks espins. *Cell*. 102:377–385. http://dx.doi.org/10.1016/S0092-8674(00)00042-8